

Journal of Geophysical Research: Solid Earth

RESEARCH ARTICLE

10.1002/2013JB010867

Key Points:

- Introducing distance-dependent seismicity sampling for b value analysis
- Identifying and mapping nonlinear frequency-magnitude distributions
- Resolving spatial b value heterogeneity along Californian faults

Correspondence to:

T. Tormann,
thessa.tormann@sed.ethz.ch

Citation:

Tormann, T., S. Wiemer, and A. Mignan (2014), Systematic survey of high-resolution b value imaging along Californian faults: inference on asperities, *J. Geophys. Res. Solid Earth*, 119, doi:10.1002/2013JB010867.

Received 22 NOV 2013

Accepted 19 FEB 2014

Accepted article online 26 FEB 2014

Systematic survey of high-resolution b value imaging along Californian faults: Inference on asperities

T. Tormann¹, S. Wiemer¹, and A. Mignan¹¹Swiss Seismological Service, ETH Zurich, Zurich, Switzerland

Abstract Understanding and forecasting earthquake occurrences is presumably linked to understanding the stress distribution in the Earth's crust. This cannot be measured instrumentally with useful coverage. However, the size distribution of earthquakes, quantified by the Gutenberg-Richter b value, is possibly a proxy to differential stress conditions and could therewith act as a crude stress-meter wherever seismicity is observed. In this study, we improve the methodology of b value imaging for application to a high-resolution 3-D analysis of a complex fault network. In particular, we develop a distance-dependent sampling algorithm and introduce a linearity measure to restrict our output to those regions where the magnitude distribution strictly follows a power law. We assess the catalog completeness along the fault traces using the Bayesian Magnitude of Completeness method and systematically image b values for 243 major fault segments in California. We identify and report b value structures, revisiting previously published features, e.g., the Parkfield asperity, and documenting additional anomalies, e.g., along the San Andreas and Northridge faults. Combining local b values with local earthquake productivity rates, we derive probability maps for the annual potential of one or more M_6 events as indicated by the microseismicity of the last three decades. We present a physical concept of how different stressing conditions along a fault surface may lead to b value variation and explain nonlinear frequency-magnitude distributions. Detailed spatial b value information and its physical interpretation can advance our understanding of earthquake occurrence and ideally lead to improved forecasting ability.

1. Introduction

The size distribution of earthquakes, that is, the relative distribution of small to large earthquakes in a sample, is described by the Gutenberg and Richter [1944] (GR) b value: $\log N = a - bM$ (where N is the number of events $\geq M$, a is the productivity, and b is the slope). A low b value describes a data set with a large proportion of larger magnitudes, and vice versa.

The b value, estimated from the observed magnitude range (predominantly small- to medium-sized earthquakes), is a key parameter for seismic hazard analysis, since this slope of the frequency-magnitude distribution (FMD) is used to extrapolate expected recurrence rates of large and not (regularly) observed earthquakes, which dominate a region's hazard. Even small variations (e.g., ± 0.1) in b value change the expected rates of large events significantly. Most seismic hazard assessments still use average b values for large regions (e.g., the Uniform California Earthquake Rupture Forecast, Version 3 (UCERF3) model, *Field et al.*, 2013), or at best distinguish between seismotectonic zones (e.g., the 2004 Swiss Hazard Model, *Wiemer et al.* [2009]).

While global and regional data sets often closely follow an FMD with $b = 1$, detailed studies in the last two decades have shown substantial variations in b on a local scale of several kilometers. In particular, strong b value heterogeneity has been documented along selected fault segments, with asperity locations (rough partly locked and highly stressed patches on a fault plane that are likely to rupture in a larger event) being correlated to low b values [e.g., *Wiemer and Wyss*, 1997; *Oncel and Wyss*, 2000; *Schorlemmer et al.*, 2004a; *Schorlemmer and Wiemer*, 2005; *Tormann et al.*, 2012]. Geothermal and volcanic regions, presumably characterized by high fluid flow and high pore pressures, feature high b values [e.g., *Wiemer et al.*, 1998; *Wyss et al.*, 2001; *Bachmann et al.*, 2012]. Classified by their focal mechanisms, thrust earthquakes from several catalogs in different regions of the world have been shown to generally be associated to lower b values than strike slip and normal earthquakes [e.g., *Schorlemmer et al.*, 2005; *Gulia and Wiemer*, 2010; *Yang et al.*, 2012]. Furthermore, b values have been found to systematically decrease with depth [*Mori and Abercrombie*, 1997;

Gerstenberger et al., 2001] down to the brittle-ductile transition zone, below which the trend reverses [*Spada et al.*, 2013].

While there is no conclusive proof available and some researchers interpret measured b value variation as mostly uncertainty representation [e.g., *Amorese et al.*, 2010], all these above observations strongly suggest that the negative correlation between b values and differential stress, which has been repeatedly measured in laboratory experiments over several decades [e.g., *Scholz*, 1968; *Amitrano*, 2003; *Goebel et al.*, 2012; *Goebel et al.*, 2013], holds true for real-world earthquakes. Mapping b values may be used as a crude stress-meter to visualize the relative stress distribution in the Earth's crust. In that mission, the several published case studies that identify asperities along isolated fault segments need to be complemented by a larger scale and systematic investigation of the applicability of the b value stress-meter to a complex fault network. What spatial coverage on anomalous regions can be resolved? How stable and meaningful are the case study results? Are the resolved structures consistent with previous and independent structural knowledge? In this study, we present a systematic survey along all major documented Californian faults. To do so, we reevaluate and advance the technique of cross-sectional b value imaging: a number of simplifications that were accepted in the beginnings of b value imaging are still state-of-the-art practice in recent case studies but not applicable to systematic analyses of complex settings.

2. Improved Technique of High-Resolution Cross-Sectional b Value Imaging

2.1. Essentials of Cross-Sectional b Value Imaging

Since the first cross-sectional b value study by *Wiemer and Wyss* [1997], a number of case studies [e.g., *Wyss et al.*, 2000; *Wyss*, 2001a; *Oncel and Wyss*, 2000; *Schorlemmer et al.*, 2004a; *Wiemer and Wyss*, 2002; *Westerhaus et al.*, 2002; *Tormann et al.*, 2012] have been carried out along different fault segments and resulted in a standardized method to map b values along a cross section of a fault:

1. Select a plane vertical grid centered on the fault trace, e.g., with 1 km spacing.
2. Project all earthquakes that are located inside a chosen swath either side of the fault trace (e.g., width of 5 km) onto the grid.
3. Select a minimum number of events, N_{\min} , required to attempt the b value calculation. The more events a data sample includes, the more robust is the estimate of the b value [e.g., *Bender*, 1983; *Wiemer and Wyss*, 1997; *Wiemer and Wyss*, 2002; *Amorese et al.*, 2010]. Monte Carlo sampling and bootstrapping of real data as well as analysis of synthetic catalogs shows that the error in b is large for small numbers of events and decreases rapidly to approximately 15% for 50 events and to less than 10% for more than 150 events, reaching about 3% for 1000 events (numbers represent 1σ and are of the same order as the standard error estimate proposed by *Shi and Bolt* [1982]). Therefore, if the studied differences in b are large, 50 events are sufficient for establishing statistically significant differences and are widely used as N_{\min} .
4. For each grid node, use either the closest N events or all events from inside a constant search radius R (corresponding to cylindrical sampling volumes). Use sufficiently finer grid spacing than sampling extent around each node (e.g., 1 versus 5 km) to ensure enough overlapping to preserve independence of the choice of the grid. The larger R , the more events will be included, that is, the more nodes will reach N_{\min} and be used. But larger search radii will lose information on the small-scale heterogeneity.
5. Calculate a local b value for all grid nodes with more than N_{\min} events above M_c within R km using the maximum likelihood b value estimate derived by *Aki* [1965] and the standard error following *Shi and Bolt* [1982].

2.2. 3-D Distance-Weighted Seismicity Sampling

Sampling seismicity for cross-sectional b value analysis is a three-component issue. First, with the increasing availability of 3-D fault geometry data sets, e.g., for California, the projection of all earthquakes onto a vertical plane connecting two end points of the surface trace is an unnecessary loss of detail. Second, the width of a fault, i.e., how far off-fault earthquakes should be regarded relevant for (or produced by) the fault's stress field and therefore be included for the local b value calculation, is not naturally given, and the choice of a particular width is always subjective and hard to validate or invalidate. In some cases of largely isolated fault segments with clearly associated seismicity (e.g., Parkfield), this decision is fairly straightforward. However, for segments that are less isolated, i.e., close in space to another fault, or in regions of relatively homogeneous earthquake density, it is hard to tell which earthquake might be related to what fault [e.g., *Ouillon and Sornette*, 2011]. Furthermore, it is probably "unphysical" to regard earthquakes that are, for example, 1, 3, and 5 km away from the fault trace as equally related, while the next quake, which happens to be 100 m

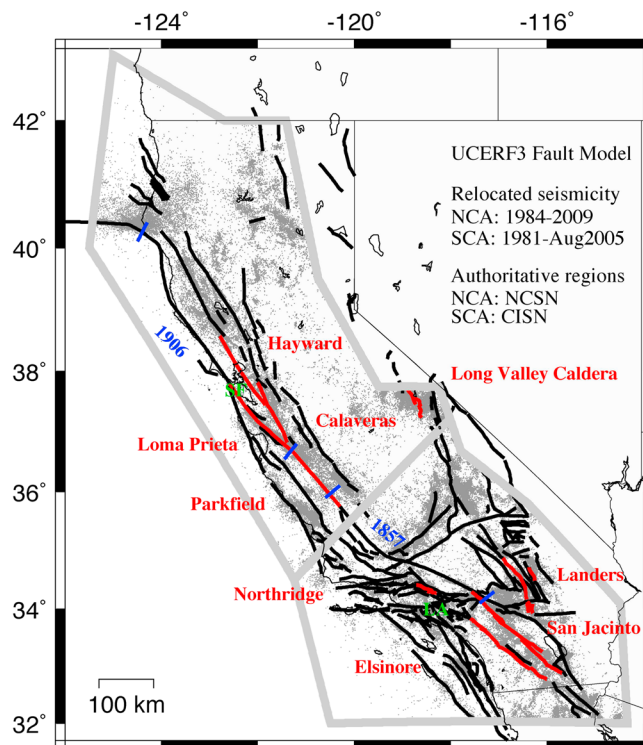


Figure 1. Map of California showing authoritative regions (grey polygons) of the northern Californian (NCA) and southern Californian (SCA) seismic networks (NCSN and CISN, respectively), earthquake data from the relocated catalogs, and the surface traces of the applied fault model. Those faults for which we present detailed cross-sectional analysis are shown in red. Blue markers indicate the approximate extents of the 1906 San Francisco and 1857 Fort Tejon earthquakes. Green: locations of San Francisco and Los Angeles.

farther out, should not relate to the fault at all. And third, that physical question of how important an earthquake is for the representation of the local stress field, based on the earthquake's distance to the location, repeats for the decision on what sampling radius to use around each grid node. Either of the two sampling methods (using a search radius or the closest N events) regards all events fulfilling the criterion equally important and does not count anything outside the search criteria.

We propose an alternative concept for b value imaging, which does not fix whether an earthquake belongs to a fault deterministically but weighs its influence depending on its distance from the fault. By calculating the 3-D distance between each earthquake and fault grid node, we avoid the choice of a fault width and the traditional search radius but assign each earthquake a distance-dependent weight. For the computation of the FMD and its b value we therefore do not count numbers of earthquakes but their weights, that is, their importance to the considered node, depending on a distance-dependent decay function.

In order to investigate the potential resolution gain of different sampling algorithms, we perform a numerical experiment: we build a semisynthetic seismicity catalog based on the Advanced National Seismic System (ANSS) catalog from the last 30 years for the Parkfield section of the San Andreas Fault (Figure 1). We use the empirical locations of $M \geq 1.3$ events, and therewith realistic local productivity rates, which strongly vary throughout the segment from densely clustered to sparse. We then assume a true b value structure along the 70 km long and 20 km deep fault segment (Figure 2a). The structure features a rather large body of low b value of 0.5 and two smaller rectangles of high b values of 1.3 and 1.8 in a high- and a low-productivity area, respectively. Those three anomalies are surrounded by a background b value of 1. We resample the empirical magnitudes by drawing a new magnitude for each event according to the earthquake's location from distributions of the assumed true local b value. We then apply different seismicity sampling algorithms to the simulated catalog, trying to retrieve the synthetic b value distribution. Since the magnitude assignment is a random process, we simulate 500 magnitudes for each event and analyze the b value cross sections calculated from each of these 500 catalogs. The different sampling approaches that we test are as follows:

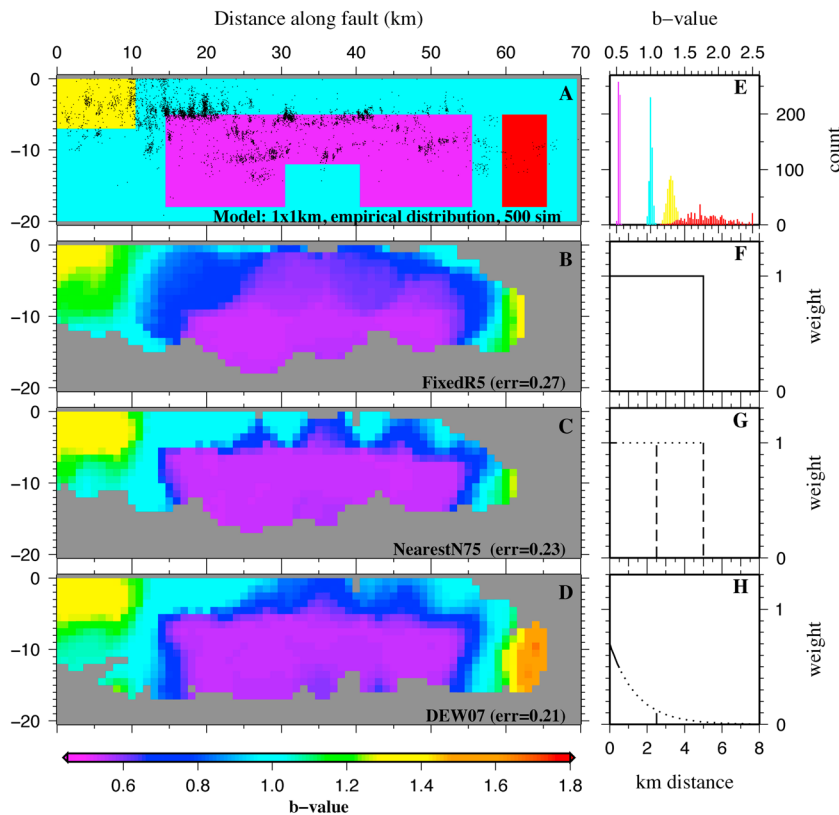


Figure 2. (a) Synthetic b value structure and empirical $M \geq 1.3$ earthquake locations (black dots) along the Parkfield segment of the San Andreas fault. (b–d) The b values as recovered with the three different sampling algorithms. (e) Distribution of measured b values of the earthquakes inside each volume, for the 500 drawn magnitude distributions. (f) Sketch of the *FixedR5* method: each event within 5 km distance gets equal weight. (g) Sketch of the *NearestN75* method: each earthquake gets equal weight, solid part (0–0.3 km) marks shortest distance in which 75 earthquakes have been found, and dashed lines show the two applied limits: at least one earthquake needs to be located closer than 2.5 km, and maximum radius = 5 km. (h) Sketch of the *DEW07* method: each earthquake gets weight according to its distance, shortest distance in which 150 (maximum allowed number of events) were found is 0.4 km, and at least one event needs to be located closer than 2.5 km (dashed line).

1. *FixedR* considers the earthquakes within a fixed radius. We use all events that are located within R km from the grid node and calculate a local b value whenever the number of selected events exceeds the chosen minimum number for computation, which we set to $N_{\min} = 50$ (the same N_{\min} for all runs of all sampling algorithms). In 0.5 km steps, we test a range of $3 \leq R \leq 6.5$ km.
2. *NearestN* considers the closest N earthquakes. For each grid node we select the closest N events, $N \geq N_{\min}$, to calculate a b value. We introduce two limiting conditions. First, we enforce a maximum radius, that is, if N events cannot be sampled within the maximum radius, $r_{\max} = 5$ km, of the grid node; we do not calculate a b value. And second, we require at least one event to be located within a close distance of the considered grid node; otherwise we exclude the grid node, arguing that the value for this grid node would be artificial, since it stems only from events far away. We set the minimum distance to 2.5 km. In intervals of 25, we test the range $N_{\min} = 50 \leq N \leq 225$.
3. *DEW* method is the Distance Exponential Weighted method. For the distance weight we applied three different decay functions: the normal, exponential, and Pareto distributions. We find that the exponential distribution performs constantly the best, and we decide to concentrate on this function. For each earthquake we calculate its distance, d , to the analyzed grid node and compute its corresponding weight according to the following formula:

$$\text{weight}(d) = \lambda e^{-\lambda d} \quad (1)$$

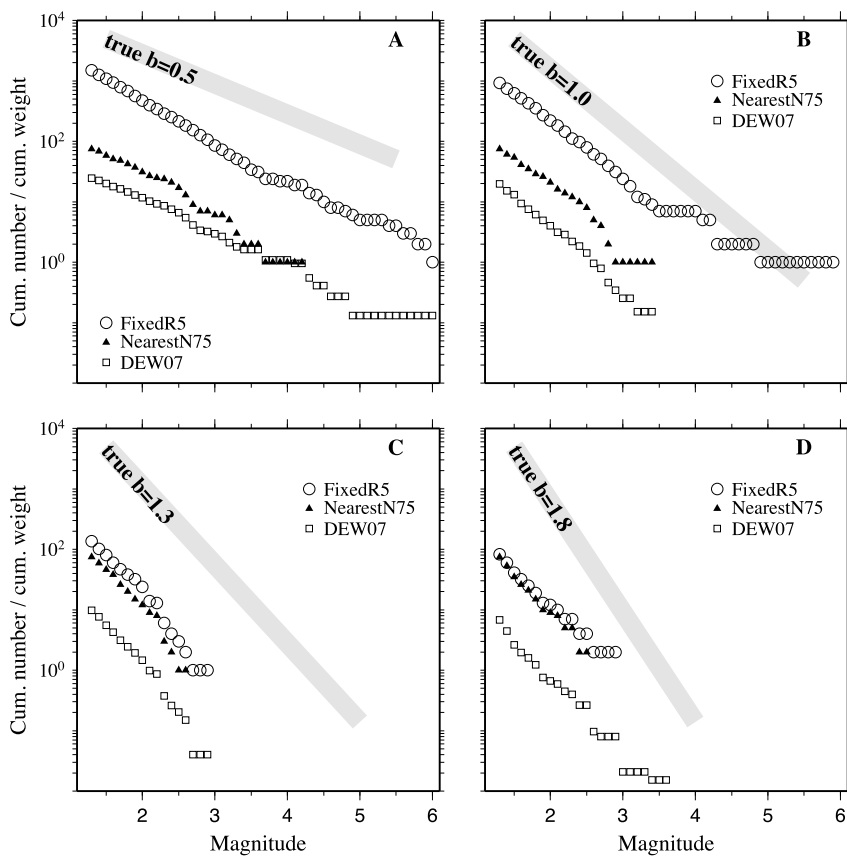


Figure 3. FMDs for the three sampling methods for four selected nodes from different true b value volumes: (a) 0.5, (b) 1.0, (c) 1.3, and (d) 1.8. For FixedR5 and NearestN75 sampling, the cumulative distributions represent the numbers of events sampled; the lower numbers for the DEW07 sampling are due to not counting each event as 1 but only a fraction between 0 and 0.7, depending on the distance. This distribution shows the slope but cannot be directly used to recover the a value. This is done either in keeping track of the total number of sampled events for each node or by subsequent rescaling of the normalized weighted density of events.

We test a range of λ values between 0.3 and 1 in 0.1 intervals. Having calculated the weight for each earthquake, we then compute the sum of the weights for each magnitude bin, find the mean magnitude from this distribution, and calculate a maximum likelihood b value according to Aki [1965].

Similarly to the NearestN method, we have applied limits. To reduce computing time, we do not calculate the miniature weights for all far away earthquakes but only for events within a maximum radius, which we set to $r_{\max} = 7.5$ km. The weight at 7.5 km distance is already less than half a percent for the preferred decay function. In this sampling approach, we also aim to avoid calculating b values on deserted nodes and require at least one event to be located within 2.5 km. And finally, to acknowledge higher resolution where possible, we enforce a maximum number of events considered: once $N = 150$ is reached, the events farther away are neglected.

As demonstrated for four selected grid nodes of different true b values (Figure 3) the GR scaling holds for the distance-weighted FMD. By definition, the cumulative sum of the weights is smaller than the cumulative number of used events; that is, to correctly recover the a value, the weighted distribution can be scaled to the total number of events used at each grid node. Figure 3 shows the pure weighted FMDs without this rescaling.

In order to identify which of the sampling algorithms is superior in retrieving the known input structure, we first find for each approach the most successful parameter value. We run 500 simulations and compare the calculated b value cross section against the real b value distribution. We take the very simple measure of the sum of the local deviations and penalize for empty grid nodes. If N is the total number of grid nodes

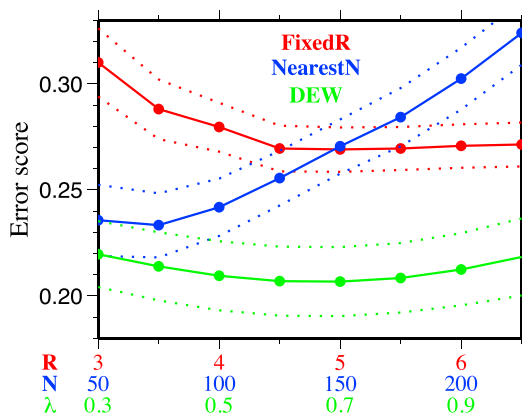


Figure 4. Error scores (mean with standard deviation) from the 500 runs for the three different sampling algorithms for different parameter choices. Lowest error scores represent best fitting data; DEW is most successful in recovering the structure.

methods with their optimized parameters, Figure 4 shows that the DEW07 yields the statistically significantly lowest and therewith best score (0.21 ± 0.01), followed by the NearestN75 algorithm (0.23 ± 0.01), and the most commonly used FixedR5 (0.27 ± 0.01). Figure 4 demonstrates that although we chose the most successful parameter for each algorithm, the superior ability of the DEW algorithm in retrieving the given structure is insensitive to the choice of the parameters. We visualize the resolution power of the different methods by showing their b value cross-section reproductions (Figures 2b–2d). For each sampling algorithm, we show at each grid node the mean local b value over the 500 runs calculated from the optimal parameter.

We note that this ranking of the algorithms and in particular the identified optimal parameter choices are specific to the chosen seismicity distribution together with the synthetic true b value structure. For different settings, those parameter values might change. Nevertheless, we constructed the test structure such that it features anomalies in high as well as low seismicity regions, since such varying seismicity density is what we find along faults, and the size of the major anomaly is of the size of a moderate earthquake rupture area, which is what this study aims to image. Furthermore, as shown in Figure 4, the choice of λ is not critical in this setting, and we additionally retrieved the same $\lambda = 0.7$ for other semisynthetic settings that we tried. In summary, we are confident that the DEW07 sampling is capable of resolving features at higher resolution than the traditional FixedR5 method, even without optimizing λ separately for each fault segment.

2.3. Magnitude of Completeness

Since we consider in this study all major known Californian faults, we have to choose a strategy of estimating appropriate magnitudes of completeness, M_c , which vary throughout the state. Estimating M_c too low and therefore using incomplete parts of the FMD leads to artificially low b value estimates [Woessner and Wiemer, 2005; Mignan and Woessner, 2012]. On the other hand, choosing M_c too high reduces the set of usable data, that is, the spatial resolution, and increases the uncertainty in b unnecessarily. To optimize our b value coverage and conserve the quality, we choose to calculate the M_c locally along the surface traces of the faults.

We map M_c by using the Bayesian Magnitude of Completeness (BMC) method introduced by Mignan *et al.* [2011]. Following that approach, which uses the robustness of Bayes' theorem by combining local M_c observations with prior information based on the density of seismic stations, we create two BMC maps for California, based on a $0.1^\circ \times 0.1^\circ$ longitude-latitude grid (Figure 5a) and on fault nodes (Figure 5b). We use default parameters to obtain the M_c^{obs} map and then calibrate the model to the northern and southern California M_c^{obs} values to compute M_c^{pred} and M_c^{post} (i.e., BMC map, Figure 5) for both regions. Results are then combined by mosaic mapping. A full description of the applied method is given in Appendix A. For the local b value analysis, we select at each node the highest BMC value within the search radius that we apply, that is, within 7.5 km, and add an extra 0.2 to be conservative and avoid bias toward lower b values. BMC provides a time-independent long-term estimate of M_c . Potential minor temporal variation is accounted for by the extra 0.2 that we add. To account for significant changes, which are always observed throughout

($N = 1400$) and n the number of grid nodes for which a b value has been calculated, we determine the score as follows:

$$\text{score} = \frac{N}{n} * \sum \frac{\text{abs}(\text{true values} - \text{test values})}{n} \quad (2)$$

The smaller the score value, the better the match between the tested and true b value distributions.

After the 500 runs, we take for each of the sampling methods and each of their parameter values the mean of the 500 score results and find the minimum score per sampling algorithm. We find the NearestN algorithm to perform best for $N = 75$ and the FixedR for $R = 5$ km (Figure 4). The distance decay is most successful with an exponential decay function with $\lambda = 0.7$. Comparing the scores of the three

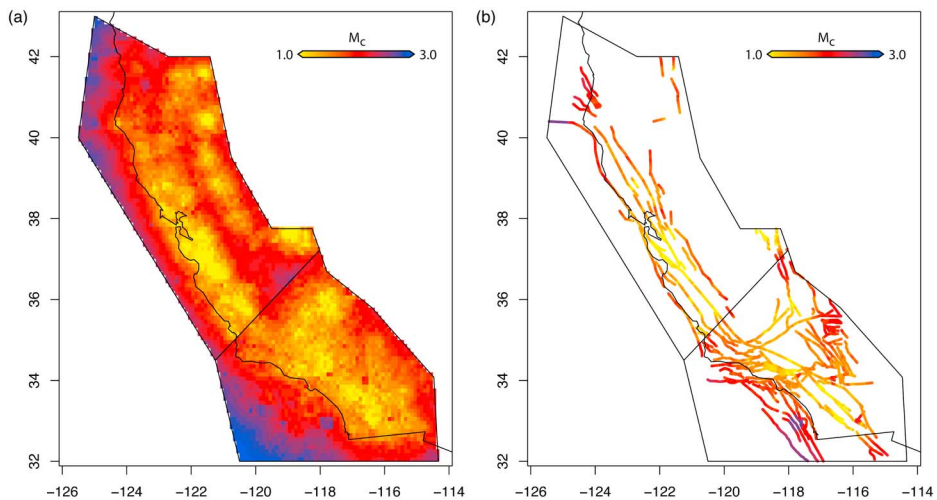


Figure 5. M_c maps for California, based on the BMC method: (a) grid based and (b) fault based.

aftershock sequences of major events, we individually reassess and fix M_c as documented for each case. For those detailed analyses, we always exclude the very first days after the main shock.

2.4. Linearity Assessment of Local b Value Estimates

This study calculates local b values from roughly three decades of Californian seismicity (all events above M_c) and interprets them in terms of stress and likelihood differences for large events. Where the small earthquakes follow a low b value, we expect the chances for large events, M_{6+} , to be higher than in an equally productive volume following a high b value.

Visual inspection of local FMDs shows that not all samples are as “well behaved” or linear as required for a sensible extrapolation to large magnitudes; that is, not everywhere does the local FMD follow a power law. We introduce a Non Linearity Index (NLIndex) to assess whether a locally observed earthquake sample follows the GR distribution and can be used to derive expected rates for M_{6+} events.

The algorithm judges the linearity of a sample catalog based on the b value estimates for different cut-off magnitudes, starting at M_c and increasing up to $M_{\text{cut}50}$, which is the highest magnitude above which $N_{\min} = 50$ events are still observed. If by this definition at least five b value estimates can be calculated, we define the NLIndex as the ratio of the standard deviation of these b value estimates divided by the largest individual uncertainty [Shi and Bolt, 1982] in the single b value estimates.

If $\text{NLIndex} \leq 1$, the underlying FMD is considered linear and can be extrapolated to large magnitudes using the observed b value. If NLIndex is higher than 1, the FMD is not linear and the b value cannot be used to extrapolate to large magnitudes. In a second step, we additionally analyze the trend in the b value development with increasing cutoff magnitude, which allows a distinction whether the b value, if used for extrapolation, would overpredict or underpredict the rates of large-magnitude events. Figure 6 visualizes how the NLIndex works for different sample catalogs.

If the nonlinear nature of the FMDs is concentrated at the lower magnitude end and the larger magnitudes scale linearly, the NLIndex can be used to identify an alternative cutoff magnitude $M_{\text{altco}} > M_c$, as long as the volume is productive enough and features more than 50 events above $M_{\text{altco}} + 0.5$, and estimate that slope of the upper end of the magnitude distribution.

2.5. Translation Into M_{6+} Probabilities

For grid nodes with $\text{NLIndex} \leq 1$, we derive from the observed productivity of earthquakes at this node the annualized a value, a_{ann} , which we normalize to the average rupture area of an M_6 target event [Wells and Coppersmith, 1994]. Together with the estimated local b value, we calculate the expected recurrence time, Tr , of a magnitude M_6 or greater event:

$$Tr(M_{6+}) = \frac{1}{10^{a_{\text{ann}} - b*6}} \quad (3)$$

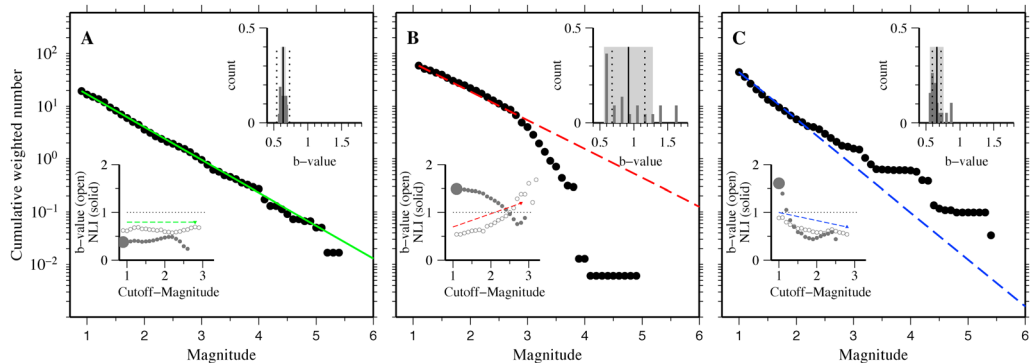


Figure 6. Comparison between FMDs and NLIndex for three different categories. (lower insets) The b values (open circles) and the NLIndex (solid circles) for different cutoff magnitudes, i.e., the first value is the NLIndex for the full FMD and its b value, the second would be the index and b value if the FMD was cut 0.1 magnitudes higher, etc. The distribution is accepted if the first NLIndex is below 1. In some cases, an increase in the cutoff magnitude can extract a linear distribution from a rejected FMD at low M_c (in Figures 6b and 6c). The slope of the b values indicates whether the misfits overpredict or underpredict large-magnitude rates. (upper insets) Histogram of the different b values for different cutoff magnitudes, together with their mean (solid line) and standard variation (grey shading); dashed line shows the largest Shi and Bolt error associated with any of the individual b value estimates. As long as the dashed lines are outside the shading, the FMD is classified linear. (a) An accepted linear FMD; the NLIndex is below 1 for all cutoff magnitudes, and the b value is stable with increasing cutoff magnitude. (b) A rejected nonlinear FMD, for which the NLIndex is greater than 1 and the b values strongly increase with increasing magnitude; that is, the positive slope of the b value signal indicates an *overestimate* of large-magnitude rates. (c) A rejected nonlinear FMD, for which the NLIndex is greater than 1 at low cutoff magnitudes but decreases and would accept the distribution as linear for higher cutoff magnitude and associated lower b value estimate and the b values decrease with increasing magnitude; that is, the negative slope of the b value signal indicates an *underestimate* of large-magnitude rates.

This expected recurrence time can be translated into the expected annual probability of occurrence of one or more $M6$ or greater events using

$$Pr(M6+) = 1 - e^{-1/Tr(M6+)} \quad (4)$$

3. Systematic Survey of Californian Faults

3.1. Data

With this study we intend to achieve the highest possible spatial resolution and reliability of systematic b value estimates for California's faults, which requires the highest possible data quality. We use the best available fault model and relocated earthquake data sets for northern and southern California, NCA and SCA, respectively. We restrict our analysis to remain inside the authoritative regions of the northern and southern seismic networks, NCSN and CISN, respectively, as given on <http://www.ncedc.org/anss/anss-detail.html> (Figure 1).

3.1.1. Relocated Earthquake Catalogs

For NCA, we use the double difference relocated catalog compiled by *Waldbauer and Schaff* [2008], which covers the time between 1 January 1984 and 31 December 2009. It uses all earthquakes, which have been recorded by seven or more stations, implying that about one quarter of the events in the original NCSN catalog are not reported in the relocated data set [Waldbauer and Schaff, 2008]. These events are predominantly small events, which did not trigger enough stations. Because systematically disregarding small events will, if they include events above the M_c , introduce a bias toward lower b values, we merge the relocated catalog with the nonrelocated NCSN data. Those events reported in the original catalog, but not in the relocated, are added to our data set and consequently have less precise locations. We apply a magnitude cutoff of 0.5, leaving us with 478,019 events, about 82% of which are given with high-precision locations.

For SCA, *Hauksson et al.* [2012] provide a waveform relocated earthquake catalog from 1 January 1981 to 30 June 2011. This data set is complete, because contrary to the NCA catalog, events that could not be relocated are flagged and included in the catalog.

In SCA, the introduction of the new uniform Californian local magnitude, M_L , scale [Uhrhammer et al., 2011] causes a substantial change in the statistics of the magnitude distribution for small events with $M \leq 2.3$ [Tormann et al., 2010]. Among other effects, this change also mimics a significant decrease in b value, which

is why we have to restrict our data to one magnitude scale only. The relocated catalog reports the old magnitude scale up to September 2005 and from then onward the new magnitude scale. Since the newly computed data set is generally too short for our purpose, and to avoid man-made artifacts in our estimates, we use for SCA only the pre-September 2005 data. The data set includes 380,579 events inside the authoritative region with $M \geq 0.5$.

The same new M_L scale was introduced to NCA in May 2009 but did not affect the statistics of microearthquakes, since M_L in NCA is only calculated for $M3+$ earthquakes and the scaling between the old and the new scale is stable above that threshold. For NCA we can therefore use the full available data set as described above.

3.1.2. Fault Model

To calculate b value cross sections along all parameterized faults in California, we use a recent fault model compiled by the Working Group on California Earthquake Probabilities (WGCEP) during the development of the Uniform California Earthquake Rupture Forecast, Version 3 (UCERF3, *Field et al.*, 2013). The model is a modified and updated version of the fault information from the UCERF2 model [*Field et al.*, 2008] and provides detailed information on the faults' geometries including dip. We use three-dimensional grid points for 243 Californian fault sections (see Figure 1 for surface traces). We interpolate the grids for the different segments to approximately 1 km spacing along strike and with depth, resulting in about 240,000 grid points.

We calculate the b values in two subsets, the authoritative regions of the northern and southern seismic networks, restricting not only the catalogs but also the fault grid to those nodes inside the regions. In particular, that means that the fault segments, which cross the border between the two regions, are split with respect to their location relative to the authoritative regions.

3.2. Method

For each of the 3-D fault grid points within the authoritative regions of the NCSN and CISN, we sample the related seismicity using the DEW07 algorithm. Whenever we find more than 50 events above the maximum local M_c value from within the search radius of 7.5 km and at least one event within 2.5 km distance, we calculate a weighted b value following *Aki* [1965]. We note that most b value estimates are based on much more than 50 events. We do not apply a maximum number of events constraint to facilitate the estimation of the associated local a values and enable the application of the NLIndex filter, which requires at least 50 events above $M_c+0.5$. Excluding estimates identified as nonlinear, we determine from the remaining overall set of 11,928 NCA and 26,737 SCA b values the median values as reference "normal b " for the selected catalogs, that is, $b_{\text{median}}^{\text{NCA}} = 0.94$ and $b_{\text{median}}^{\text{SCA}} = 0.99$. For the nearly 26,000 "well-defined," i.e., linear (NLIndex ≤ 1) b values, in California, we translate the local a and b values into $M6+$ probabilities.

3.3. Results and Discussion

3.3.1. Cross-Sectional View Along Selected Fault Segments

3.3.1.1. San Andreas Fault: San Francisco to Parkfield, NCA

The San Andreas fault shows different seismic behavior along its segments, from mega ruptures such as the 1906 San Francisco and the 1857 Fort Tejon earthquakes (Figure 1) and full interseismic locking along those segments to the freely slipping creeping section, which steadily moves aseismically with approximately plate velocity—and two differently behaving transition zones between the locked and creeping segments: the Santa Cruz segment at the northern end, which ruptured in the 1989 $M7$ Loma Prieta earthquake, and the Parkfield segment at the southern end of the creeping zone. The Parkfield segment is probably the most extensively studied fault segment in terms of b values worldwide [*Wiemer and Wyss*, 1997; *Schorlemmer et al.*, 2004a, 2004b; *Schorlemmer and Wiemer*, 2005; *Tormann et al.*, 2012, 2013]. *Wiemer and Wyss* [1997] and *Schorlemmer et al.* [2004a] mapped a distinct low b value structure in the rupture area of the repeating moderate Parkfield earthquakes, and *Schorlemmer and Wiemer* [2005] showed that this b value anomaly based on the pre-2004 data postcasts the slip and aftershock extent of the 2004 main shock. Analysis of b value after that event has shown that the magnitude distribution is very stable throughout the seismic cycle, i.e., the overall stress levels along that segment are not much altered by the $M6$ class events [*Tormann et al.*, 2012]. The 1989 $M7$ Loma Prieta earthquake on the northern transition zone, on the other hand, changed the stressing conditions significantly, as can be resolved by b values, which were low before the main shock and have drastically increased afterward [*Tormann et al.*, 2012]. Although loading conditions would certainly be especially interesting for the segments that are known to rupture in very large events, these segments

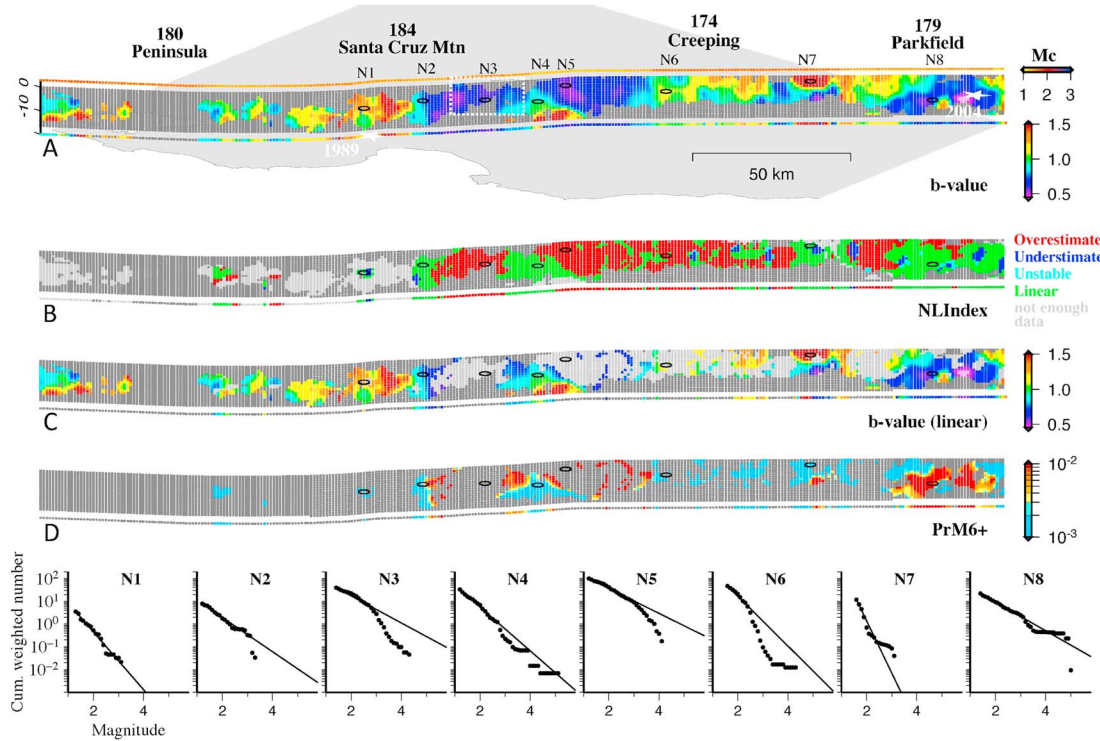


Figure 7. Cross-sectional analysis of the San Andreas fault between San Francisco and Parkfield. (a) All resolved local b values for the period January 1993 to December 2009; line along the top indicates locally applied M_c values; stars show locations of the 1989 M_7 Loma Prieta and 2004 M_6 Parkfield earthquakes; box indicates region of repeated M_5 -equivalent slow slip events and historic M_6 seismicity cluster; black circles labeled N1–N8 indicate nodes for which FMDs are shown on the bottom: N1, N2, N4, N7, and N8 are examples of stable b values, and N3, N5, and N6 are examples of nonlinear FMDs. (b) Linearity assessment of the local FMDs. (c) The b values for all nodes that are not nonlinear, that is, either linear or too few events to assess. (d) For all linear nodes: local annual probabilities for one or more M_6 or larger events to occur. Each cross section's translation via the surface trace projection is shown along the bottom trace.

of the San Andreas fault have in the last few decades not produced enough earthquakes to assess local b values.

Here we present b values between the two locked 1906 and 1857 segments, that is, from San Francisco to Parkfield, covering the creeping segment and both transition zones (Figure 7). Following the findings of Tormann et al. [2012], we restrict the time period for this fault to 1993 onward and reproduce the previous observations described above (Figure 7). While the first frame shows all resolved b values, the following frames for this and further faults will not show b values that have been identified as nonlinear by the NLIndex (second frame). Translation into probabilities will only be performed on linear nodes, i.e., also disregarding nodes with too low seismicity rates to perform the linearity assessment.

Resolution north of Loma Prieta is low, and $b \approx 1$. Interestingly, the northernmost end shows higher b values at depth than in the upper 10 km, which is an inversion of the usual depth gradient [Wiemer and Wyss, 1997; Mori and Abercrombie, 1997; Gerstenberger et al., 2001; Spada et al., 2013].

A remarkable observation obtained from this study is shown in the second cross section in Figure 7, which maps the linearity of the local FMDs according to the newly introduced NLIndex. While earthquake magnitudes along the Parkfield segment, the Loma Prieta rupture zone, and the Peninsula segment are GR distributed (Figure 7 FMDs N1, N2, N4, N7, and N8), the events south of Loma Prieta and through most of the creeping segment behave differently; they do not scale according to the power law. In particular, a blunt fit to the data would overestimate rates of large events (Figure 7 FMDs N3, N5, and N6), traditional b value assessment along this segment is not meaningful in most places.

We identify an approximately 10 km long patch between the Loma Prieta rupture zone and the non-GR slow slip dominated area farther south, which features reliably scaling low b values.

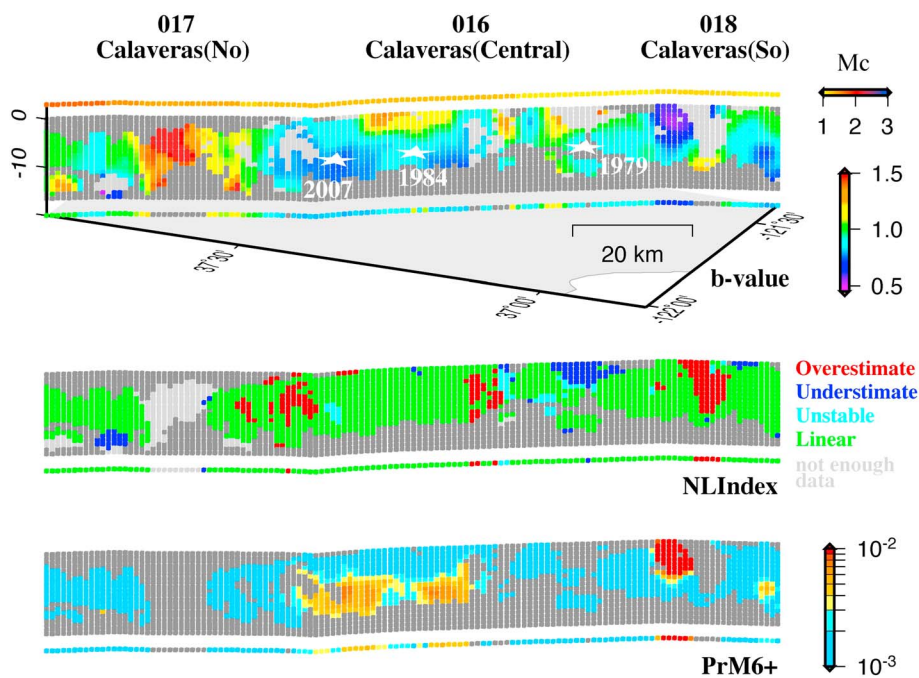


Figure 8. Cross-sectional analysis of the Calaveras fault. (top) The b value for the period January 1986 to December 2009; line along the top indicates locally applied M_c values; stars indicate the 1979 $M_5.9$ Coyote Lake, 1984 $M_6.2$ Morgan Hill, and 2007 $M_5.6$ Alumn Rock events. (middle) Linearity assessment of the local FMDs. (bottom) For all linear nodes: local annual probabilities for one or more M_6 or larger events to occur. Each cross section's translation via the surface trace projection is shown along the bottom trace.

3.3.1.2. Calaveras Fault, NCA

The Calaveras fault in the eastern San Francisco Bay Area (SFBA) has also been analyzed in terms of its b value distribution [Wiemer and Wyss, 1997]. Since it ruptured in the $M_6.2$ Morgan Hill earthquake in April 1984, Wiemer and Wyss [1997] mapped the b value distribution prior to this event and found the rupture area to be characterized by low b values. They found this pattern to be stable over the following 10 years.

We revisit this fault based on the relocated data set. Since our catalog starts in 1984, we cannot resolve any pre-main shock b values. Figure 8 shows the cross section excluding the 1984 main shock-aftershock sequence, following Wiemer and Wyss [1997] and using data from January 1986 to the end of our catalog in December 2009. We note that the results merely change, whether we include the main shock and aftershocks or not. The b values in the 1984 rupture area remain on a low level. This is consistent with the observation of Wiemer and Katsumata [1999], who documented that the aftershock b values only increased in the high slip patches and recovered their pre-main shock level within about a year. Such behavior has since also been documented for Parkfield [Tormann et al., 2012]. The Calaveras low b value volume produced another moderate shock of $M_5.6$ in October 2010, known as Alumn Rock earthquake. We map a second and even more pronounced low b value volume toward the south, on the boundary of the central and southern Calaveras fault segments, and just south of the 1979 $M_5.9$ Coyote Lake rupture (Figure 8). In this southern patch, we resolve the currently highest likelihood for M_6+ events to occur.

3.3.1.3. Hayward Fault, NCA

The Hayward fault in the SFBA is known for a diversity of different slip behaviors: exhibiting aseismic creep and abundant microseismicity, it also produced major ($M_6.5$ – 7.1) earthquakes in the past, with a mean recurrence time over the last five events of 138 years [Lienkaemper and Williams, 2007]. The last event broke in 1868 with a magnitude of 6.8 [Bakun, 1999], with an inferred approximate rupture extent of 40 km from about Oakland to about Fremont [e.g., Malservisi et al., 2005]. This seismic record together with the elapsed time makes the Hayward fault one of the most hazardous faults in California and in a very densely populated area [Brocher et al., 2008]. Several studies have already been published that assess the Hayward fault's seismic potential from different perspectives: paleoseismicity [e.g., Lienkaemper and Williams, 2007; Lienkaemper et al., 2010], geodesy [e.g., Burgmann et al., 2000; Schmidt et al., 2005], microseismicity [e.g., Wyss, 2001a],

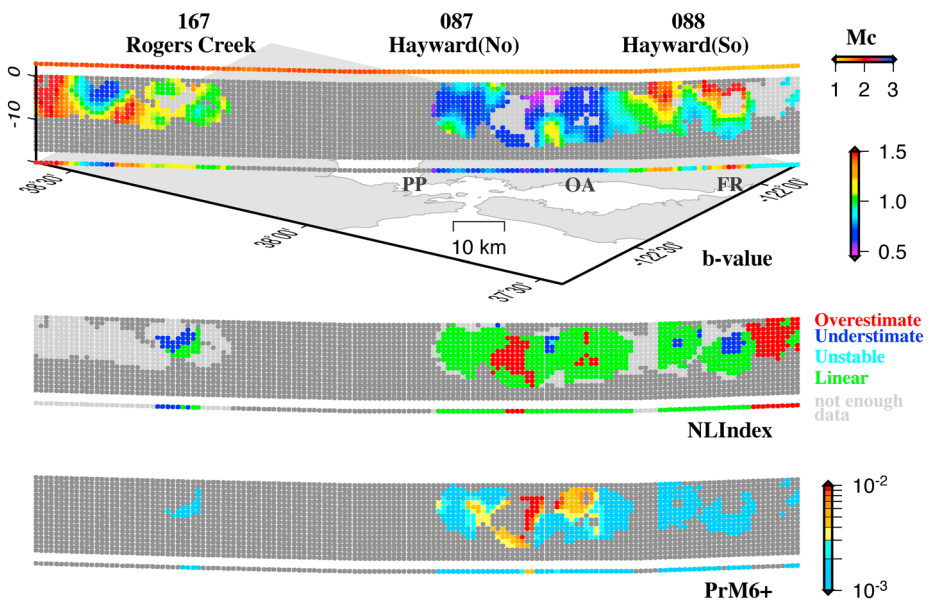


Figure 9. Cross-sectional analysis of the Hayward fault. (top) The b value for the period January 1984 to December 2009; line along the top indicates locally applied M_c values; PP, OA, and, FR indicate locations of Point Pinole, Oakland, and Fremont, respectively; the last major event ($M_{6.8}$) ruptured in 1868 from about Oakland to Fremont. (middle) Linearity assessment of the local FMDs. (bottom) for all linear nodes: local annual M_6+ probabilities. Each cross section's translation via the surface trace projection is shown along the bottom trace.

and combinations [e.g., *Malservisi et al.*, 2005; *Shirzaei et al.*, 2013]. A particular interest is to map locked patches that might exist along the fault plane and only break in larger ruptures. A study by *Wyss* [2001a] analyzed b values and local recurrence times and documented two apparently locked patches along this fault and not only along the southern segment that broke in 1868 but also toward the north, a segment that is debated on whether it is capable of producing major earthquakes or not [e.g., *Burgmann et al.*, 2000].

We revisit the fault and resolve a pronounced low b value volume of approximately 40 km length (Figure 9), which overlaps and extends northward from the northern end of the estimated 1868 rupture [*Burgmann et al.*, 2000; *Malservisi et al.*, 2005] out to Point Pinole. Farther north, b values can only be resolved along the northern half of the Rogers Creek segment, where a ~10 km wide low b value volume is imaged, surrounded by $b > 1$. The Hayward asperity location, and its apparent highest-probability center near Oakland, correlates with significantly lower ($\approx 2\text{mm/yr}$) surface creep rates measured in Oakland (on top of the asperity) compared to values farther south, where the fault creeps faster with $\approx 4\text{mm/yr}$ [*Lienkaemper et al.*, 2012] and b values are high (Figure 9). This observation is in line with a correlation between surface creep rates and asperity b values documented for Parkfield [*Tormann et al.*, 2013]. Even higher surface creep rates of $>6\text{mm/yr}$ are measured around Fremont [*Burgmann et al.*, 2000; *Malservisi et al.*, 2005], where we resolve very high b values. No creep measurements seem to be available south of Fremont, which is where our filter starts identifying nonlinear FMDs (Figure 9).

3.3.1.4. Hilton Creek and Round Valley Faults (Long Valley Caldera), NCA

The Long Valley Caldera is a tectonically complex and active volcanic system in the Eastern Sierra Nevada. Seismic activity in the area is dominated by swarms and the highest rate of moderate earthquakes in all of California over the last 150 years [*Hill and Bailey*, 1985]. The recent period of seismic unrest started in 1978, associated with a significant inflation of the caldera, and continued since with varying levels of activity and ongoing ground deformation [e.g., *Hill and Bailey*, 1985; *Sorey et al.*, 2003; *Langbein*, 2003]. Two well-recorded earthquake swarms occurred contemporaneously with episodes of geodetically documented reinflation in 1989–1990 and 1997–1998. Both episodes mark significant volcanic and seismic activity that might change the conditions within the system Long Valley Caldera. To investigate potential changes, *Wiemer et al.* [1998] analyzed the 3-D spatial and temporal variation in the size distribution of earthquakes between 1984 and 1997. They mapped patches of high b values, which indicate highly fractured crust or high pore pressures, likely in the vicinity of a magma body. They furthermore documented a distinct change in b value initiated by and following the 1989 earthquake swarm, probably related to magma intrusion.

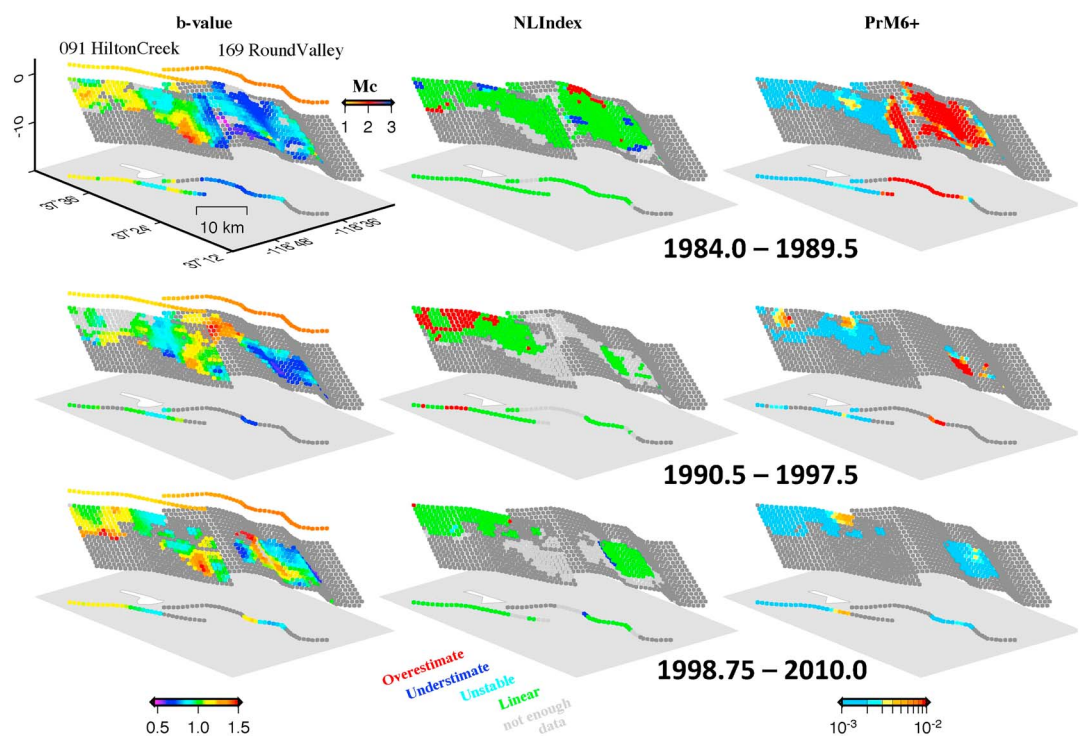


Figure 10. Cross-sectional analysis of the Hilton Creek and Round Valley faults south of Long Valley Caldera, for three time periods. (left) The b values; line along the top indicates locally applied M_c values. (middle) Linearity assessment of the local FMDs. (right) For all linear nodes: local annual M_{6+} probabilities. Each cross section's translation via the surface trace projection is shown along the bottom trace.

We map b values along the Hilton Creek and Round Valley faults, which run approximately north-south from the southern end of the caldera. We split the catalog into three time periods, before, between, and after the 1989 and 1998 inflation and swarm episodes (Figure 10). Similarly to the findings by Wiemer *et al.* [1998], we map two volumes of high b values along the Hilton Creek fault, the northern one slightly shallower than 10 km, the southern one deeper. These volumes do not appear to change during the periods of unrest and could be indicating presence of magma or fluids or more generally high pore pressures. The b values along the Round Valley fault, on the other hand, change drastically between the three periods, with low values before the 1989 swarm and then increasing values, first in the north after the 1989 swarm and later also along the southern end at depth after the 1998 swarm. Whether this new deep patch of high b values indicates significant release of accumulated tectonic stresses or rather a new dike intrusion remains speculative on the basis of the microseismicity analysis. The combination of varying activity rates and b values along the Round Valley fault results in significant differences in expected annual probabilities for moderate events (Figure 10).

3.3.1.5. Northridge, SCA

The 1994 $M_{6.8}$ Northridge earthquake ruptured a previously unknown buried thrust fault north of Los Angeles. The same area was shaken in 1971 by the $M_{7.1}$ San Fernando earthquake that ruptured another close-by thrust fault dipping in the opposite direction, i.e., to the northeast, with the Northridge fault dipping to the southwest [e.g., Mori *et al.*, 1995; Hauksson *et al.*, 1995; Carena and Suppe, 2002]. While the San Fernando earthquake ruptured the surface, the Northridge earthquake started deep at about 19 km depth and ruptured upward to about 5–7 km depth. At this depth, the San Fernando fault crosses through the fault plane of the Northridge fault, preventing it from continuing to the top. The two earthquakes overlapped in parts of their aftershock zones [Mori *et al.*, 1995]. Wiemer [2000] studied the b values from the Northridge aftershock sequence, i.e., 2 years of data, in order to assess aftershock probabilities. They found the largest aftershock ($M_{5.1}$, April 1997) to occur in a location with the highest probabilities based on previous local microaftershock a , b , and p values, the latter describing the aftershock rate decay.

We map b values for three different time periods (Figure 11). Before the 1994 earthquake, we resolve predominantly low values, although resolution is low for this early period. As documented by Wiemer [2000],

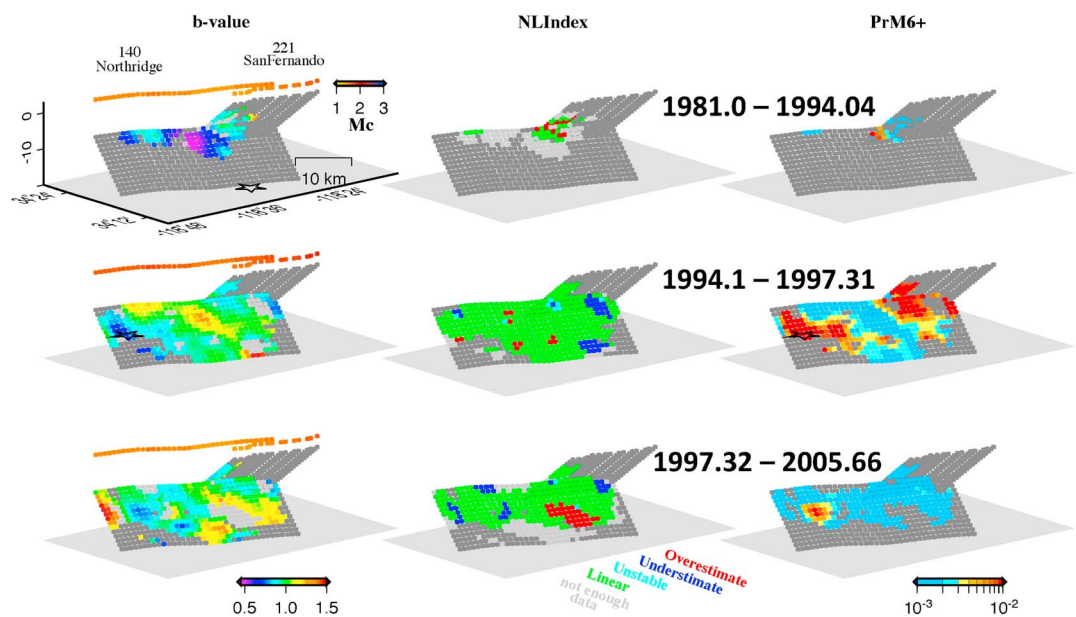


Figure 11. Cross-sectional analysis of the Northridge and San Fernando faults, for three time periods. (left) The b values; line along the top indicates locally applied M_c values; star indicates the 1994 $M_6.8$ Northridge hypocenter and the 1997 $M_5.1$ aftershock. (middle) Linearity assessment of the local FMDs. (right) For all linear nodes: local annual M_6+ probabilities.

the aftershock sequence until the 1997 $M_5.1$ aftershock is characterized by high b values in the highest slip regions, i.e., in the eastern half of the Northridge fault, while the western end still shows low b values and high probabilities. The $M_5.1$ aftershock ruptured the high-probability patch. Interestingly, the b values remain mostly low in the western part of the faults after the occurrence of this moderate shock (Figure 11), and a high-probability patch remains.

3.3.1.6. Landers/BurntMtn/EurekaPeak/JoshuaTree/HectorMine Faults, SCA

The 1992 $M_7.3$ Landers earthquake that ruptured in the eastern California shear zone is the largest earthquake in California since the seismic network started recording in the 1920s. It was preceded by the $M_6.1$ Joshua Tree earthquake 2 months before and produced a massive aftershock sequence including the close-by $M_6.5$ Big Bear earthquake 3 h after Landers and in 1999 the possibly delayed triggered $M_7.1$ Hector Mine earthquake [Freed and Lin, 2001]. Seismicity rates in large parts of California have been found to change with the occurrence of the Landers main shock, reducing activity in some parts and increasing rates in others [Hauksson *et al.*, 1993; Wyss and Wiemer, 2000]. Wiemer and Katsumata [1999], Wiemer [2000], and Wiemer and Wyss [2002] studied spatial and temporal b value variation during the aftershock sequence and along the fault. They found that (1) b values increase throughout the sequence (early days compared to roughly the first year), and (2) b values vary along the fault, with highest b values in the region of highest slip, lower b values in the nucleation area farther south, and lowest values beyond the east-west crossing Pinto Mountain fault, i.e., along the southern “extension” of the Landers fault.

We show cross sections for the Landers and Hector Mine faults and three faults to the south: the Burnt Mountain, Eureka Peak, and Joshua Tree faults (Figure 12). They are running parallel and striking north-south, extending the Landers fault beyond the east-west running Pinto Mountain fault. We do not show the latter since it has been merely involved in the aftershock sequence. We show b values from five time slices: (1) before the $M_6.3$ Joshua Tree earthquake on 23 April 1992, (2) between Joshua Tree and the $M_7.3$ Landers main shock on 28 June 1992, (3) the first half year of Landers’ aftershocks, (4) 1993 to the $M_7.1$ Hector Mine earthquake on 16 October 1999, and (5) the remainder of the catalog, i.e., 2000 to September 2005. In order to avoid underestimates in b through completeness problems, we do not analyze data for the very first days after the main shocks, and we apply a more conservative M_c constraint on the first three periods: we double the safety factor that is added to the BMC estimates for the pre-Joshua Tree period and fix M_c for the time between the two major shocks and the first half year of the Landers aftershock sequence at 2.5. While b values before the onset of the Joshua Tree and Landers sequences have not been particularly

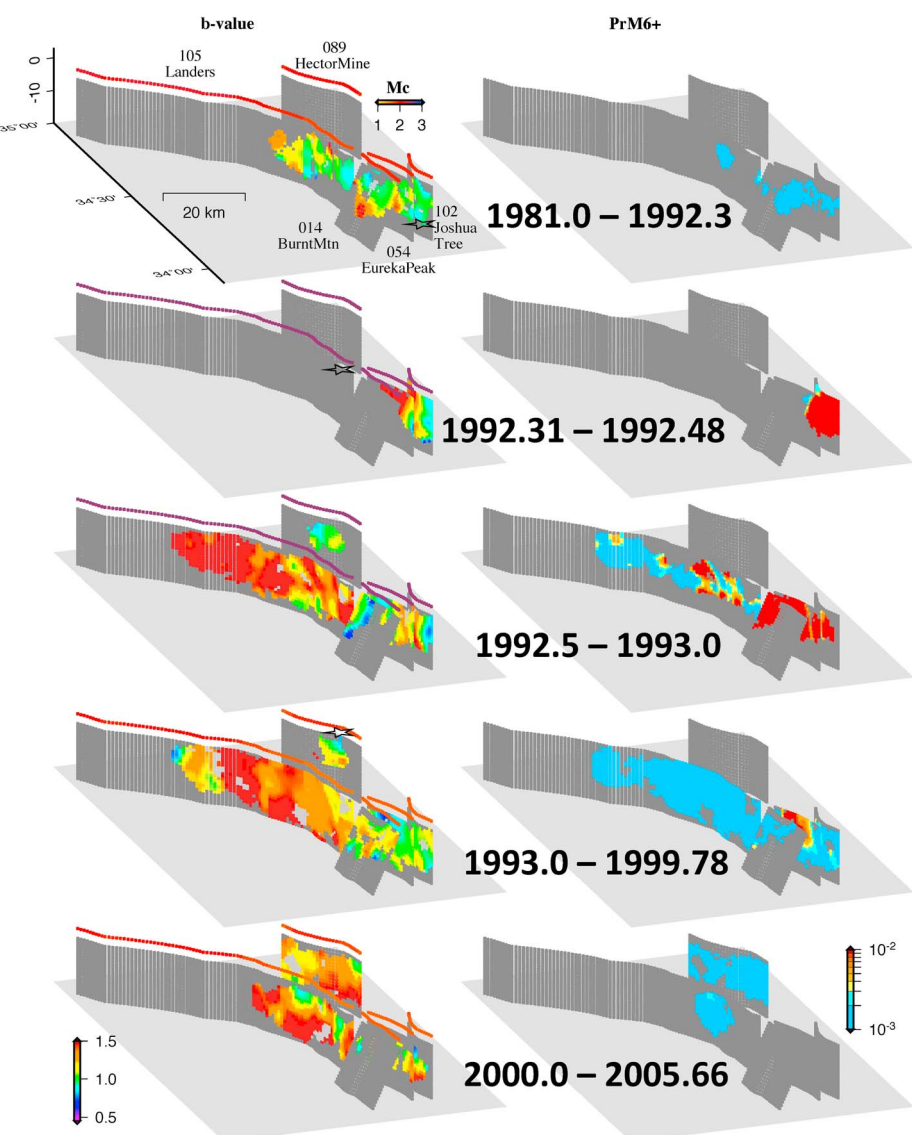


Figure 12. Cross-sectional analysis of the faults involved in the 1992 $M_{\text{w}} 6.2$ Joshua Tree, 1992 $M_{\text{w}} 7.3$ Landers, and 1999 $M_{\text{w}} 7.1$ Hector Mine earthquakes, for five time periods. (left) The b values; line along the top indicates locally applied M_c values; stars mark the locations of the three main shocks on those time slices after which they occur. (right) For all linear nodes: local annual $M_{\text{w}} 6+$ probabilities.

low in the nucleation area, such as documented among others for Loma Prieta, both main shocks still initiated in the areas of lowest resolved values. The aftershock sequence following the Joshua Tree event was tightly clustered along the Joshua Tree fault and does not allow to resolve any potential stress changes along the Landers fault. As documented by Wiemer and Katsumata [1999], the Landers aftershock b values are high, much increased compared to the first period of the catalog, and the increase is strongest in the northern section of the rupture, where slip was highest. Apart from a low b value volume which briefly develops along the Eureka Peak fault during the early aftershock sequence, the b values along the three smaller faults in the south do not change as radically, and they remain on the average level for the later part of the aftershock sequence up to Hector Mine. Following the Landers event, the Hector Mine fault is being activated sufficiently to map b values, which are around 1 with a possible decrease of the very shallow b values prior to the 1999 Hector Mine rupture and a contemporaneous increase below. Aftershock b values of the Hector Mine event are high, and activity rates along the other segments decrease, that is, the resolution of b value mapping for the last 6 years of the catalog decreases.

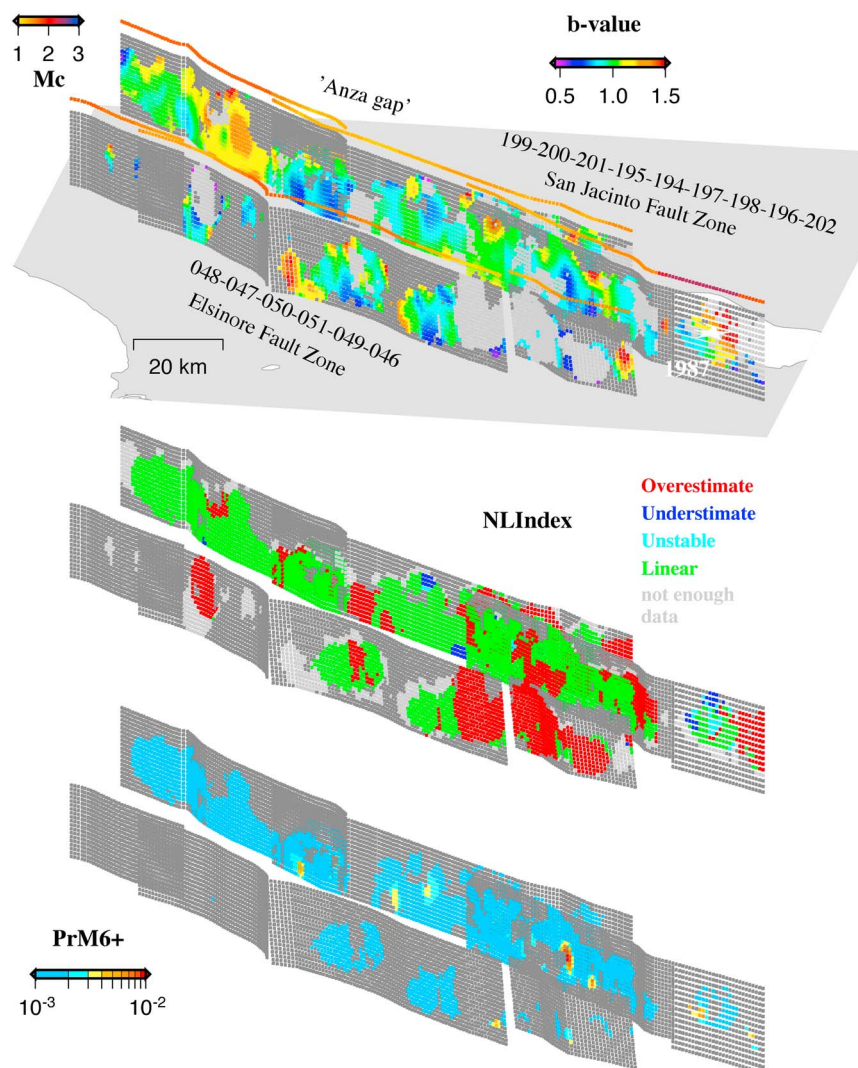


Figure 13. Cross-sectional analysis of the Elsinore and San Jacinto fault zones. (top) The b value for the period January 1981 to September 2005; star indicates the 1987 $M_6.6$ Superstition Hills event. (middle) Linearity assessment of the local FMDs. (bottom) For all linear nodes: local annual M_6+ probabilities.

3.3.1.7. San Jacinto/Elsinore Faults, SCA

The San Jacinto fault zone is a microseismically very active structure, which is additionally known to have produced a number of moderate earthquakes in historical times, eight since 1899 according to *Sanders* [1993]. *Wyss et al.* [2000] have studied b values along the San Jacinto and Elsinore fault zones and derived local recurrence times. They mapped several asperity structures, seen a little in the b values, but more clearly in the local recurrence time estimates, which they related to rupture extents of historical moderate events. With high confidence, they claim a correlation of the two: out of six historical main shocks that ruptured along the studied part of the fault, four were associated with asperities resolved in the local recurrence time maps. *Wdowinsky* [2009] studied seismic and geodetic data to infer the locking depth along the San Jacinto fault and conclude on its hazard potential. He suggested that the fault is characterized by deep creep, such that below 10 km the fault releases its accumulated strain by many small earthquakes and aseismic creep. This would reduce the area that could rupture in larger magnitudes to the upper 10 km of the fault, and since earthquake magnitudes scale with the rupture area, *Wdowinsky* [2009] argues that this explains the only observed moderate-sized magnitudes along the San Jacinto fault, i.e., the fault might not be able to produce anything larger.

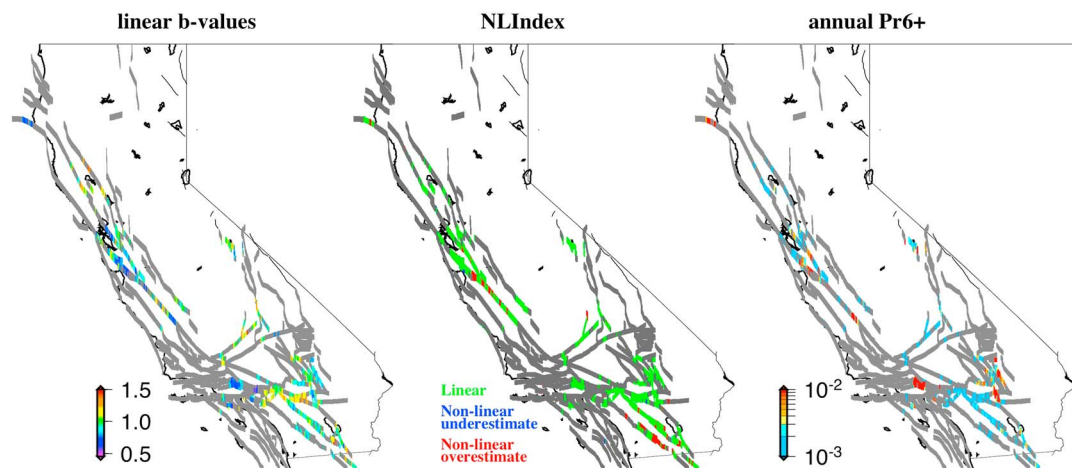


Figure 14. Surface trace projections of the study results: linear b values, linearity classes, and annual M_{6+} probabilities, for the full time periods of the northern and southern relocated catalogs, 1984.0–2010.0 and 1981.0–2005.66, respectively.

Revisiting the two fault zones, we also resolve spatial variation in b values along both the San Jacinto fault and the Elsinore fault (Figure 13). In particular, we confirm the low b value volume along the northern end of the central San Jacinto fault [Wyss et al., 2000]. This is consistent with the independent and 30 year old suggestion of a 20 km long highly locked fault patch, a seismic slip gap, the so-called the “Anza gap” [Sanders and Kanamori, 1984]. This fault segment has not ruptured in a larger earthquake since at least 1892, and no aseismic creep has been observed on the surface, while the surrounding fault patches suggest a seismogenic nature and stress accumulation. A second low b value volume is located farther south. The southernmost section features high b values; the seismicity record in this area is dominated by the 1987 $M_{6.6}$ Superstition Hill earthquake and its aftershocks. The deep creep mechanism as suggested by Wdowinsky [2009] would in terms of b values expect high b values below 10 km depth. Indeed, for the central section of the San Jacinto fault, between the two low b value volumes, b values are higher at depth than in the upper part of the fault.

Resolution in b value mapping along the Elsinore fault is much lower, especially if restricted to well-behaved FMDs. In this case we cannot reproduce the asperity structure documented by Wyss et al. [2000], since the northern low b value volume is not rated reliable: the low b values only describe the data for the magnitude range 1.5–2.2 and overestimate rates for larger magnitudes. The FMD breaks at around $M_{2.2}$, a magnitude well above completeness level.

3.3.2. Mapview: Surface Trace Projection

For the mapview presentation of the resolved b value variation along faults, we introduce in an interpretative step a surface trace projection. Though being somewhat arbitrary in its definition, it allows us to systematically visualize the locations of resolved b value anomalies along all the faults in California. Moving along the surface trace of a fault segment’s grid, we analyze at each 1 km step the values of the grid’s column at this point. Whenever a column is dominated by linear scaling, i.e., more linear than nonlinear nodes, we count all linear low and high b value grid nodes, i.e., below and above the b_{median} of all nodes for NCA and SCA, respectively. To avoid being misled by outliers, we use only those categories with at least three nodes in that column and determine which of the two categories dominates in numbers of nodes, i.e., low or high b value nodes. We, accordingly, take either the mean of the low b values or the mean of the high b values and display that b value on the surface trace above the column. Figures 8–10 demonstrate the surface traces extracted for those fault segments shown in cross-sectional detail.

Figure 14 shows all surface trace projections of dominant b values in California, together with the determined linearity class and, for power law distributed magnitudes, the translation into annual probabilities of M_{6+} events.

3.3.2.1. Nonlinearity Locations

In most regions, local seismicity in California is described well by the GR power law scaling. Systematic nonlinearity is observed in NCA along the Santa Cruz and Creeping segments of the San Andreas fault and at

the southern end of the Hayward fault (all these regions show significant aseismic deformation) and in SCA along the Elsinore fault.

3.3.2.2. The b Values

As demonstrated in the set of cross sections before, b values vary significantly along California's faults, clearly identifying not only regional but local differences. Apart from low b values along the offshore part of the northern San Andreas fault, b values north of San Francisco are generally higher than average. The SFBA faults feature low b values at least along some sections, indicating high stress accumulation and confirming independent assessments that conclude high future rupture probabilities especially for the Hayward fault [Field *et al.*, 2008]. The San Andreas fault stands out with several sections of low b values, which in part are classified as nonreliable, that is, south of Loma Prieta and along the Creeping section. Parkfield marks the southern end of where we can resolve b values along the Central San Andreas fault and shows low b values. With the exception of the Northridge area, b values in SCA appear to be generally high. Previously observed low b values along the Elsinore fault mostly disappear because of nonlinearity.

Two aspects need to be kept in mind regarding these maps: (1) The absolute and relative b values should only be compared within either NCA or SCA, since the networks use different magnitude scaling relations, and b values might be different just due to technical and processing decisions rather than them being physically related. (2) The time periods for the two authoritative regions are different, and in this view the data shown are an average over local temporal b value variation that was resolved as documented in the previous section.

3.3.2.3. M_{6+} Asperities

For linear nodes, we translate the local a and b values into annual probability estimates for M_{6+} events. Local b values have been successfully used to map and help understand local fault structure and identify presumably highly stressed fault patches. The probability map also includes information on current activity levels and therewith some concept of the likelihood of triggering a bigger event: the more events are being triggered overall, the more likely one of them might grow larger—scaled by the local b value. This concept is probably not applicable to all faults, in particular not to fully locked segments that are activated without warning in a major earthquake. Assuming that microseismically active faults can be assessed like that, the probability map indicates the places where faults are not only stressed but also significantly at unrest, so large events seem most likely. Locations with higher probability are the SFBA faults and Parkfield. The large main shock-aftershock sequences of Loma Prieta, Landers, and Northridge strongly influence the probabilities, and those locations are more realistically assessed for individually restricted postaftershock time periods. Of these, only the Northridge area appears to have some notable probability beyond the 1994 sequence.

It is important to note regarding these maps that there could be lots of red along the many grey traces of the faults, which either are not productive enough in terms of small events or could not be confirmed as featuring linear FMDs.

3.3.3. Limitations of Microseismicity-Derived Information

Microseismicity has already been suggested to be indicative of destructive seismic activity. Parkfield is the most prominent example, where the $M1$ – $M3$ earthquakes correctly forecast the observed occurrence rates of $M6$ class events [Wiemer and Wyss, 1997; Schorlemmer *et al.*, 2004a; Tormann *et al.*, 2012]. Along the North Anatolian fault, retrospective analysis of microseismicity prior to the 1999 $M7.4$ Izmit earthquake has highlighted a low b value zone, which was the asperity that ruptured in the main shock [Westerhaus *et al.*, 2002].

On the other hand, information derived from the small earthquakes is limited for several reasons. One that we tried to address in this study is the linearity of the FMD, which might not always hold when very local data are considered. In those regions where the calculated slope of a nonlinear distribution cannot be trusted, b value analysis cannot tell much about the occurrence of large events.

This is obviously also the case for the segments of faults that currently—or ever—do not produce sufficient small-magnitude earthquakes to estimate a representative size distribution, such as the long segments of the San Andreas fault, which are known to have ruptured in mega earthquakes in 1857 and 1906. Over the last few decades at least (since modern instruments would have detected them) those known hazardous structures have not revealed themselves and their characteristics through microseismicity, which is why they do not show on our maps, although they certainly participate in, if not dominate, the current hazard potential in California.

Microseismicity-derived “asperity” maps, such as the ones shown in this paper (in terms of b values and probabilities), have to be interpreted with caution, since they lack information where no or too few small earthquakes have been recorded. These gaps are not to be interpreted as irrelevant: while some of them might relate to aseismic and nonhazardous regions, some of the gaps might even represent the “big players” in terms of future earthquake hazard, and to date there is no technique to differentiate the two.

3.3.4. New Insights Into the Physics of Fault Segments

Several studies have provided detailed b value analysis for single fault segments and suggested the idea that b value patterns can visualize structural properties of a fault segment, in particular the relative stress distribution. Such differences in local stress accumulation could likely be routed in structural and material properties, reflecting fault strength. Our systematic study could identify a relatively large number of sites where strong local heterogeneity is observed. General patterns can be inferred, such as (1) b value variation does not appear random but forms along-fault structures that can be related to otherwise inferred properties, such as locked segments mapped by slip inversion models, (2) some moderate to large earthquakes are observed to rupture in regions of previously low b values, (3) b values increase during major aftershock sequences, and (4) postaftershock b values fall into either of two categories: either they remain on a long-lasting high level, such as in the Loma Prieta or Landers cases, or they relatively quickly return to pre-main shock b values, such as in the Parkfield and Calaveras cases. Differentiating this postaftershock behavior can be used to indicate the influence of a specific main shock on the overall local stress field. The systematically resolved structures from this study provide a rich data base to independently relate them to other features and data sets in separate studies, hopefully understanding more details and general truths about California’s faults. The observation of high b values at depth along the San Jacinto fault, for example, is not necessarily a proof of the suggested deep creep [Wdowinsky, 2009], but it could be consistent with it and might help to assess the hazard potential of that fault. However, not the full San Jacinto fault features the high b values at depth, in particular the Anza gap low b value volume extends through the full depth, suggesting that high stresses do build up at least in parts of the lower fault as well. Furthermore, it remains an open question whether the higher b value volumes at depth represent a large enough difference in stresses for those parts of the fault not to participate in a potential larger rupture [Kaneko et al., 2010; Noda and Lapusta, 2013].

Nonlinearity of local FMDs as identified by this study is a new parameter derived from the size distribution of earthquakes that might provide additional insight into the physics of affected faults. While at this point there is no common explanation or understanding of what causes nonlinearity, we suggest a mechanism in the following subsection which if confirmed by different means will help to interpret this new type of information on local stressing conditions and tell more about how faults work.

3.3.5. Advanced Understanding of b

Numerous studies have already shown significant spatial variability in b values on different scales, and we resolve high heterogeneity along California’s faults. We furthermore demonstrate systematically in this study that b value patterns seem to separate into two classes, those that are stable through time, such as in Parkfield or Morgan Hill, and those that show strong variation through time, such as after the Loma Prieta or Landers earthquakes or in the Long Valley Caldera—and this variation holds beyond the pure aftershock activity. That is, whether from the full seismicity record or a subset of nonaftershocks (a declustered catalog), b values are not generally constant through time as often assumed, e.g., in probabilistic seismic hazard analysis.

Observations of spatial b value variation have been successfully related to and explained by differential stress gradients, for example, when imaging otherwise derived locked patches of faults, when observing a high correlation between b values and main shock slip patterns or aftershock distributions, or when measuring a generic b value-depth gradient. Each of our observations in this study is consistent with the hypothesis of a negative b -stress correlation, building the most systematic data set to date for a regional analysis to confirm that relationship.

While the negative correlation between b and differential stress is a robust observation, the physical details of the interactions remain to be understood: What role does local fault strength play? Could it govern the first-order observed spatial b value variation, that is, local differential stress accumulation? What role does the absolute differential stress level play versus the relative level compared to the strength? Could it explain observed b value variation between different faulting regimes? What roles do tectonic loading, aseismic creep, and coseismic stress releases of varying stress drops play? Could they dominate the second-order

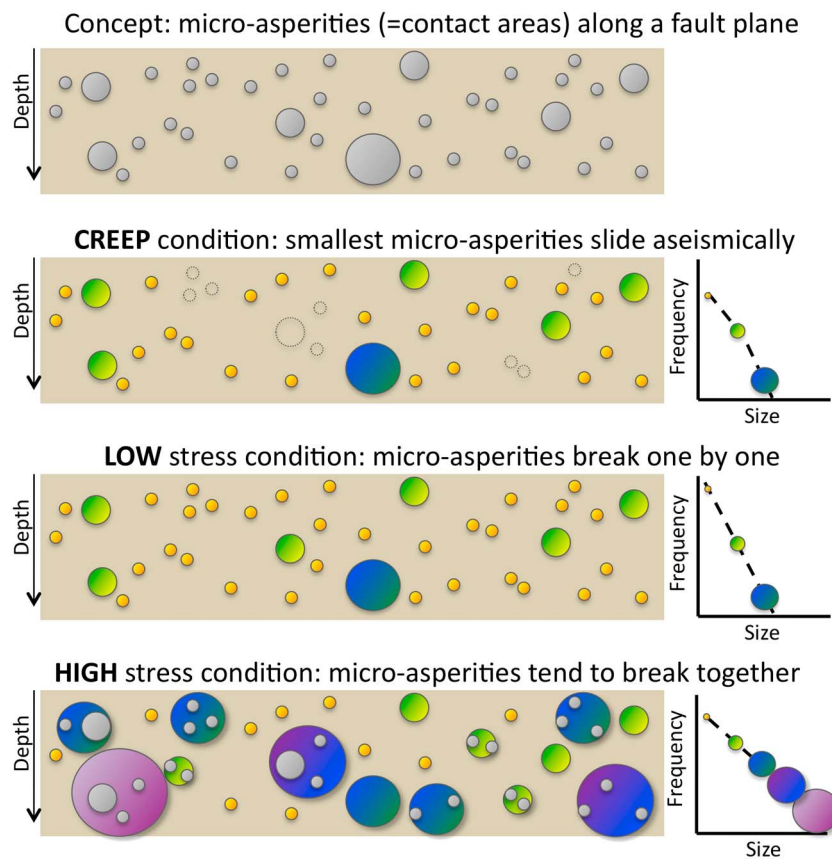


Figure 15. Cartoon illustrating a scenario of how a rough fault surface, featuring a number of different sized microasperities (symbolized by different colors), tends to break under different stress regimes, producing different linear b values and nonlinear FMDs. Open circles represent aseismically sliding asperities, i.e., events which are missing in the FMD.

observed temporal stability in some and variation in other places? How do fluids change the system? Answers to these questions are speculative to date. Different mechanistic models have been and are being developed that approach some of these questions with classical fracture mechanics and friction concepts [e.g., Scholz, 1968; Ampuero *et al.*, 2006; Rippberger *et al.*, 2007; Johnson, 2010; Dublanchet *et al.*, 2013].

Figure 15 shows an intuitive cartoon of a possible simplistic scenario how different stress regimes—either along fault or through time—could physically lead to different b values. It illustrates the concept that has also been proposed by Tormann *et al.* [2013] and which builds on the long suggested [e.g., Lay and Kanamori, 1981] understanding of a fault surface as a distribution of microasperities, contact areas between the two blocks that have higher resistance, also used in the above mentioned mechanistic models. In low stress conditions, those microasperities tend to break each on its own, producing a high number of small- and only few up to medium-sized events, resulting in a high b value. In high stress conditions, the same distribution of microasperities behaves differently: more often several of the individual patches break together, producing fewer small- and more medium-sized and also some larger ruptures, resulting in a lower b value. This conceptual framework can also explain the observed nonlinearity: if by some mechanism, e.g., higher pore pressures, the fraction between the two blocks is reduced to less than “low stress conditions,” some or more of the microasperities start sliding aseismically (presumably the smaller ones to a higher degree first); their associated seismic events are “missing” in the FMD, creating a break. If only few and the smallest of the microasperities release their stress aseismically, the verification of the b value fit to the FMD suggests an underestimated M_c , an effect which is observed strongly along the creeping section (Figure 16). If more microasperities are affected, the break moves toward larger magnitudes and becomes more obvious to be something abnormal. The maximum likelihood b value fits the lower slope of the distribution above M_c , which in that scenario is “incomplete,” and does not represent a true b value. If the aseismic creep “substitutes” small events, the true seismic potential would have to be estimated from the steeper slope above the

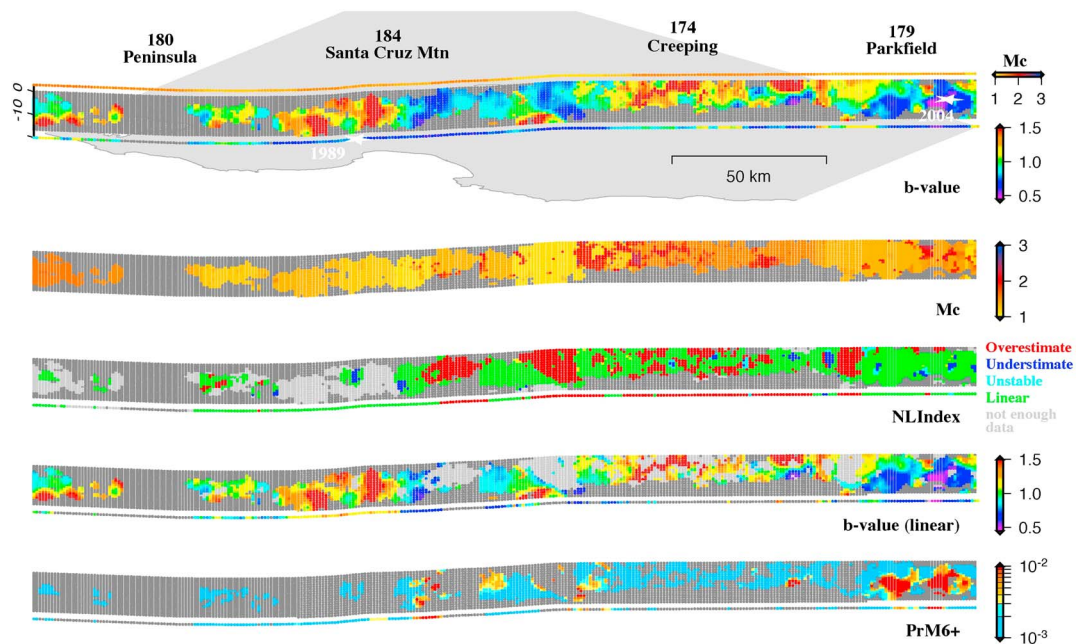


Figure 16. Cross-sectional analysis of the San Andreas fault in January 1993 to December 2009, using the NLIndex-based optimized cutoff magnitude. If a nonlinear node has enough events of a linearly scaling distribution for magnitudes above the break, the cutoff magnitude is being adjusted, fitting a b value to the upper part of the distribution. This follows the concept that smaller magnitude events might be missing, even well above the local instrumental M_c , because the relevant microasperities release their stress aseismically. (top to bottom) All resolved b values and BMC surface trace; applied cutoff magnitudes; linearity assessment; linear b values; and annual M_6+ probabilities.

break, i.e., the higher b value. We have applied this concept to b value mapping along the San Andreas fault and specifically the creeping segment, which was identified with predominantly nonlinear FMDs (Figure 16). In particular, we used the optional feature of the NLIndex filter to assess whether an increased cutoff magnitude above the suggested M_c provides a “linearized” distribution, and if so, we fitted that slope. As expected from the visual inspection of the data in Figure 7, many nodes along the creeping segment can be fitted reliably with that technique, and the b values are predominantly high, which is what to expect intuitively along a creeping segment: less potential of large-magnitude events. It is hard to rule out, though, that instead of missing small events, by some other mechanism the large events have been “prevented” during the recording time, in which case the lower b value would describe the long-term behavior more appropriately. Breaks in the FMD could also be created by swarm activity, which produces an excess of events within one or few particular magnitude bins. This can be best detected through checking noncumulative FMD plots.

3.3.6. Potential of b as Input Parameter for Seismicity Simulators

One option to use the b value details resolved along cross sections of faults is as input parameter for physics-based seismicity simulators to approximate the initial stress conditions along a fault. This rapidly growing field of seismological research is expected by many renowned researchers to play a significant role in future earthquake hazard assessment. In particular, real earthquake catalogs might to a high degree, or even completely, be replaced by simulated catalogs, since those can be generated for any time scale and thereby cover multiple cycles of the rare very big earthquakes in a considered region. Using cross-sectional b value analysis could provide realistically distributed initial stresses along complex systems [e.g., Ide and Aochi, 2013] and help develop an idea of the impact and evolution of the initial conditions.

3.3.7. Relevance for Probabilistic Seismic Hazard Assessment

Probabilistic seismic hazard assessment is concerned about the occurrence rates of large events. Due to the long recurrence times, we have no sufficient record of observations and the information has to be estimated from both the best knowledge about the geologic structures (i.e., the potential sources of future large events, their geometry, slip rates, and past activity) and the current instrumental seismicity record with its statistical characteristics. One critical parameter in extrapolating for the rates of large events is the b value, which is usually assumed to be constant through space (possibly with few very obvious

exceptions like geothermal areas) and time, and is often set to unity. As shown in this study, neither of the three assumptions apply to the Californian seismicity of the last few decades:

The b in California is not one single number as so often proposed and applied. Such simplification might need to be reconsidered on the basis of the variation documented in this study.

The b values vary strongly through space and along the fault segments, highlighting pronounced areas of higher likelihood for future rupture initiation. This variability is information that should be considered as one parameter set for hazard analysis, just as different faults are associated with different slip rates. Applying bulk mean b values is at least a loss of available information. A major challenge that remains to be solved in this context, though, is how to treat those faults that cannot be assessed in terms of b values (see section 3.3.3).

The b values vary significantly through time over the last few decades, at least in places, and suggest changing high-nucleation potential areas. To estimate current hazard, the most recent data should be considered separately, at least as one branch in the logic tree.

4. Conclusions

We introduced a new seismicity sampling algorithm, DEW, which assigns for all earthquakes a distance-dependent weight and calculates b values from the weighted FMDs. We showed for synthetic data that this sampling technique has the potential to resolve target structures for this study with more detail than “traditional” constant radius sampling. We suggest that any b value imaging study should assess whether the chosen techniques are capable of resolving structures of the anticipated size.

We introduced a linearity filter, NLIndex, which allows to assess whether local FMDs follow the power law scaling of magnitudes. Since nonlinear FMDs cannot be sensibly used to infer large-magnitude recurrence rates, we propose to only rely on b values that have been shown to adequately describe the underlying data. The NLIndex provides additional information on the nature of the misfit, that is, whether the fitted b value overpredicts or underpredicts rates of large-magnitude events. Systematic analysis of these features can potentially lead to physical explanations of why the FMDs do not follow a GR power law fit, the NLIndex possibly being an indicator for significant aseismic stress release.

Our systematic survey, using best available data quality, in particular the recently published relocated catalogs, and a homogeneous mapping technique, confirms previously reported b value phenomena throughout California (i.e., Parkfield, Loma Prieta, Calaveras, Hayward, Long Valley Caldera, Landers, Northridge, and San Jacinto) and provides more detail in most cases. This alone is a reassuring finding in that the anomalies documented by the different case studies with different techniques and available data at the time are robust structures, which likely represent meaningful insight into the stress distribution along California’s faults. The one exception for which we could not reproduce previously documented low b values is along the Elsinore fault in SCA, which is due to predominantly nonlinear scaling.

Our survey furthermore reveals low b values south of Loma Prieta and in the Northridge region. Whether an event nucleating in the area south of Loma Prieta could grow either toward the north into the Loma Prieta rupture zone or south into the aseismic deformation zone and reach moderate to large magnitudes remains speculative but not impossible [Kaneko *et al.*, 2010; Noda and Lapusta, 2013]. Toppozada *et al.* [2002] report a series of historical M_{6+} seismicity in the slow slip region between 1840 and 1899. Slightly north of Los Angeles, the Northridge region features a number of partly buried thrust faults, one of which produced the destructive 1994 $M_{6.8}$ Northridge earthquake. Only two decades before, the 1971 $M_{7.1}$ San Fernando earthquake ruptured a close-by fault. Despite those relatively large earthquakes that struck here only recently, the faults appear to remain stressed and might be capable of producing further damaging earthquakes.

Appendix A: Bayesian Magnitude of Completeness

We map M_c by using the BMC method introduced by Mignan *et al.* [2011]. This approach uses the robustness of Bayes’ Theorem by combining local M_c observations with prior information based on the density of seismic stations. In contrast with other existing FMD-based methods (see review by Mignan and Woessner [2012]), BMC provides a complete spatial coverage of M_c while avoiding oversmoothing. The method has

already been applied in Taiwan [Mignan et al., 2011], mainland China [Mignan et al., 2013], the Lesser Antilles arc [Vorobieva et al., 2013], Switzerland [Kraft et al., 2013], and Greece [Mignan and Chouliaras, 2014].

The BMC method is a two-step procedure. It consists of (1) a spatial resolution optimization to compute an observed M_c^{obs} map, where the number of M_c estimates is maximized while spatial heterogeneities in M_c are minimized, and (2) a Bayesian approach that combines observations and prior information. Mignan et al. [2011] defined the prior $M_c^{\text{pred}} = f(d, k)$ with d the distance to the k th nearest seismic station as

$$M_c(d, k) = c_1 d^{c_2} + c_3 \quad (\text{A1})$$

where parameters c_1 , c_2 , and c_3 are determined empirically. The parameter k is chosen as the minimum number of stations to be triggered for initiating the location procedure in the network, usually between 3 and 5. For Taiwan, Mignan et al. [2011] found $c_1 = 9.42$, $c_2 = 0.0598$, $c_3 = -9.60$, and a standard deviation $\sigma = 0.18$ for $k = 5$ with d in kilometers (referred to as default parameters later on). Equation (A1) has been shown to be valid in various regions, although data scattering may be high [e.g., Mignan et al., 2013] and instabilities observed at long distances [e.g., Vorobieva et al., 2013].

The first step of the BMC method, the spatial resolution optimization procedure, consists in computing $M_c^{\text{obs}}(x, y)$ from the FMD that corresponds to events located in a cylindrical volume centered on cell (x, y) of radius r

$$r = \frac{1}{2} \left[\left(\frac{c_1 d^{c_2} + \sigma}{c_1} \right)^{\frac{1}{c_2}} - \left(\frac{c_1 d^{c_2} - \sigma}{c_1} \right)^{\frac{1}{c_2}} \right] \quad (\text{A2})$$

where d , c_1 , c_2 , c_3 , and σ are the same parameters as in equation (A1). In equation (A2), σ can be interpreted as the M_c interval under which variations cannot be resolved. Note that Vorobieva et al. [2013] found a similar scaling law using a different approach. It follows that at a cell (x, y) located at $d = 50$ km from the fifth nearest station, $r = 13$ km; for $d = 100$ km, $r = 24$ km; and for $d = 200$ km, $r = 45$ km. If r is smaller than half the cell diagonal distance, the FMD is computed from all earthquakes located in that cell (highest spatial resolution). The idea that regions of homogeneous M_c are smaller in the dense parts of the seismic network than in the outer regions is in agreement with independent observations made by Mignan [2012]. This method avoids any arbitrary decision on parameter r and any oversmoothing that could corrupt M_c estimates [Mignan et al., 2011; Mignan and Woessner, 2012].

M_c is computed as the magnitude bin with the maximum number of events, which has been shown to be valid for homogeneous data sets described by an angular FMD [Mignan, 2012]. In BMC, M_c^{obs} is the mean of M_c values obtained from 200 bootstrap FMD samples and σ_0 is the associated standard error. Event sets composed of at least four events are used since Mignan et al. [2011] demonstrated that for small sample sizes, (1) uncertainty estimates based on bootstrapping are still reliable and (2) the observed large fluctuations of σ_0 are an accurate reflection of how well a particular sample of magnitudes can constrain M_c . Note that this is only valid for an angular FMD. For other FMD shapes, M_c estimation requires a larger set of events to reach a stable value.

The second step of BMC consists in merging prior information (equation (A1)) with observations, based on Bayes' Theorem. Following Mignan et al. [2011], we calculate the posterior M_c^{post} as

$$M_c^{\text{post}} = \frac{M_c^{\text{pred}} \sigma_0^2 + M_c^{\text{obs}} \sigma^2}{\sigma^2 + \sigma_0^2} \quad (\text{A3})$$

which is the average of the predicted and observed M_c , weighted according to their respective uncertainties. The posterior standard deviation σ_{post} is given by

$$\sigma_{\text{post}} = \sqrt{\frac{\sigma^2 \sigma_0^2}{\sigma^2 + \sigma_0^2}} \quad (\text{A4})$$

It follows that observations M_c^{obs} have more weight in regions of low uncertainty (low σ_0), while prior information has more weight in region of high uncertainty. In regions where there is no observation, the prior M_c^{pred} is used.

We create two BMC maps for California, based on a $0.1^\circ \times 0.1^\circ$ longitude-latitude grid (Figure 5a) and based on fault nodes (Figure 5b). Equation (A1) with default parameters and $k = 5$ is used to obtain the M_c^{obs} map

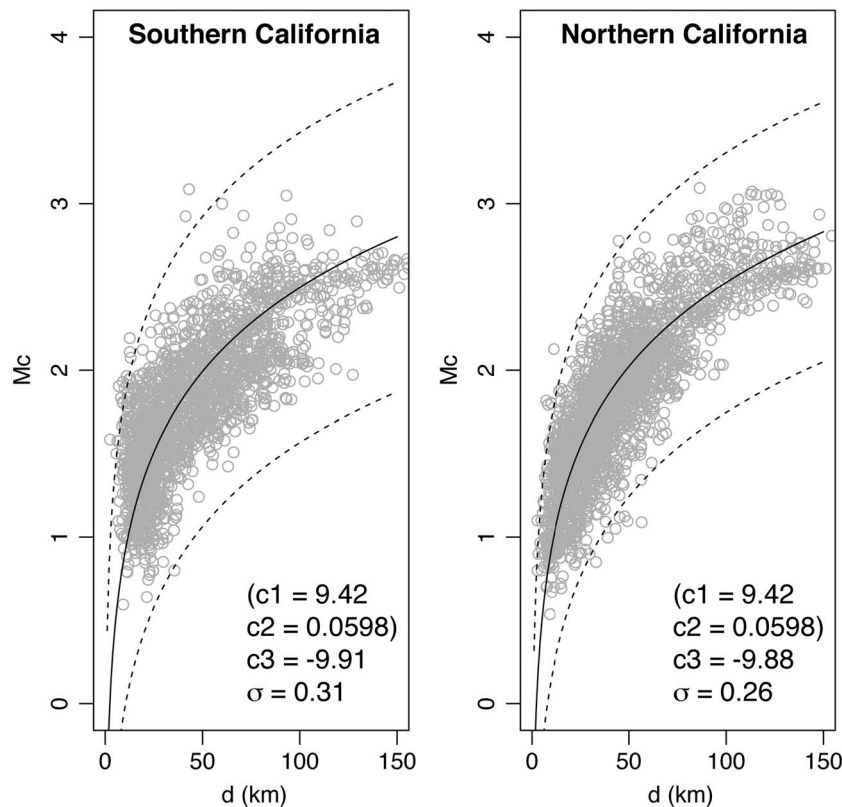


Figure A1. M_c versus distance d to the fifth nearest seismic station in SCA and NCA. The model (solid line) is based on equation (A1). The parameters given in parentheses are fixed and correspond to default values. Other parameters are determined from the data. Dashed lines show the $\pm 3\sigma$ envelopes of the model.

(not shown). Equation (A1) is then calibrated to the NCA and SCA M_c^{obs} values to compute M_c^{pred} (Figure A1, map not shown) and M_c^{post} (i.e., BMC map, Figure 5) for both regions. Results are then combined by mosaic mapping. Due to the relatively high data scattering (Figure A1), equation (A1) is not directly fitted to the data; instead, the default model is calibrated to the Californian data by shifting parameter c_3 to minimize the residual (i.e., $c_1 = 9.42$ and $c_2 = 0.0598$ fixed, $c_3 = -9.91$ and $\sigma = 0.31$ obtained for SCA, $c_3 = -9.88$ and $\sigma = 0.25$ obtained for NCA) [Mignan et al., 2013].

Acknowledgments

We thank J. L. Hardebeck, J. Woessner, A. Guilhem, S. Hiemer, and P. Dublanchet for discussions and feedback on the manuscript. We thank J.-P. Ampuero, an anonymous reviewer, and the Associate Editor for constructive comments. We thank the WGCEP for sharing the fault data base. Earthquake data were obtained from <http://www.ideo.columbia.edu/felixw/NCAeqDD/> and <http://www.ncedc.org/anss/catalog-search.html> for NCA and <http://www.data.scec.org/research-tools/alt-2011-dd-hauksson-yang-shearer.html> for SCA. Figures were produced with the generic mapping tools <http://gmt.soest.hawaii.edu/>. Part of this study was funded through SNF grant PMPDP2 134174.

References

- Aki, K. (1965), Maximum likelihood estimate of b in the formula $\log N = a - bM$ and its confidence limits, *Bull. Earthquake Res. Inst.*, 43, 237–239.
- Amitrano, D. (2003), Brittle-ductile transition and associated seismicity: Experimental and numerical studies and relationship with the b value, *J. Geophys. Res.*, 108(B1), 2044, doi:10.1029/2001JB000680.
- Amorese, D., J.-R. Grasso, and P. Rydelek (2010), On varying b -values with depth: Results from computer-intensive tests for southern California, *Geophys. J. Int.*, 180, 347–360, doi:10.1111/j.1365-246X.2009.04414.x.
- Ampuero, J.-P., J. Rippberger, and P. Mai (2006), Properties of dynamic earthquake ruptures with heterogeneous stress drop, in *Earthquakes: Radiated Energy and the Physics of Faulting*, *Geophys. Monogr. Ser.*, vol. 170, edited by R. Abercrombie, et al., pp. 255–261, AGU, Washington, D. C., doi:10.1029/170GM25.
- Bachmann, C., S. Wiemer, B. Goertz-Allmann, and J. Woessner (2012), Influence of pore-pressure on the event-size distribution of induced earthquakes, *Geophys. Res. Lett.*, 39, L09302, doi:10.1029/2012GL051480.
- Bakun, W. (1999), Seismic activity of the San Francisco Bay region, *Bull. Seismol. Soc. Am.*, 89(3), 764–784.
- Bender, B. (1983), Maximum likelihood estimation of b -values for magnitude grouped data, *Bull. Seismol. Soc. Am.*, 73, 831–851.
- Brocher, T., J. Boatwright, J. Lienkaemper, C. Prentice, D. Schwartz, and H. Bundock (2008), The Hayward fault—Is it due for a repeat of the powerful 1868 earthquake. *Fact Sheet 2008-3019*, US Geological Survey.
- Burgmann, R., D. Schmidt, R. Nadeau, M. d'Alessio, E. Fielding, D. Manaker, T. McEvilly, and M. Murray (2000), Earthquake potential along the northern Hayward fault, California, *Science*, 289, 1178–1182, doi:10.1126/science.289.5482.1178.
- Carena, S., and J. Suppe (2002), Three-dimensional imaging of active structures using earthquake aftershocks: The Northridge thrust, California, *J. Struct. Geol.*, 24, 887–904, doi:10.1016/S0191-8141(01)00110-9.
- Dublanchet, P., P. Bernard, and P. Favreau (2013), Creep modulation of Omori law generated by a Coulomb stress perturbation in a 3-D-rate-and-state asperity model, *J. Geophys. Res. Solid Earth*, 118, 4774–4793, doi:10.1002/jgrb.50311.
- Field, E., et al. (2013), Uniform California earthquake rupture forecast, version 3 (UCERF3)—The time-independent model, *U.S. Geol. Surv. Open File Rep.*, 2013–1165. [Available at <http://pubs.usgs.gov/of/2013/1165/>.]

- Field, N., et al. (2008), The Uniform California Earthquake Rupture Forecast, Version 2, *Open-file Report 2007-1437*, US Geological Survey.
- Freed, A., and J. Lin (2001), Delayed triggering of the 1999 Hector Mine earthquake by viscoelastic stress transfer, *Nature*, **411**, 180–183, doi:10.1038/35075548.
- Gerstenberger, M., S. Wiemer, and D. Giardini (2001), A systematic test of the hypothesis that the *b* value varies with depth in California, *Geophys. Res. Lett.*, **28**, 57–60.
- Goebel, T., D. Schorlemmer, T. Becker, G. Dresen, and C. Sammis (2013), Acoustic emissions document stress changes over many seismic cycles in stick-slip experiments, *Geophys. Res. Lett.*, **40**, 2049–2054, doi:10.1002/grl.50507.
- Goebel, T., et al. (2012), Identifying fault heterogeneity through mapping spatial anomalies in acoustic emission statistics, *J. Geophys. Res.*, **117**, B03310, doi:10.1029/2011JB008763.
- Gulia, L., and S. Wiemer (2010), The influence of tectonic regimes on the earthquake size distribution: A case study for Italy, *Geophys. Res. Lett.*, **37**, L10305, doi:10.1029/2010GL043066.
- Gutenberg, B., and C. Richter (1944), Frequency of earthquakes in California, *Bull. Seismol. Soc. Am.*, **34**, 185–188.
- Hauksson, E., L. Jones, K. Hutton, and D. Eberhart-Phillips (1993), The 1992 Landers earthquake sequence: Seismological observations, *J. Geophys. Res.*, **98(B11)**, 19,835–19,858.
- Hauksson, E., L. Jones, and K. Hutton (1995), The 1994 Northridge earthquake sequence: Seismological and tectonic aspects, *J. Geophys. Res.*, **100(B7)**, 12,335–12,355.
- Hauksson, E., W. Yang, and P. Shearer (2012), Waveform relocated earthquake catalog for southern California (1981 to June 2011), *Bull. Seismol. Soc. Am.*, **102(5)**, 2239–2244, doi:10.1785/0120120010.
- Hill, D., and R. Bailey (1985), Active tectonic and magmatic processes beneath Long Valley Caldera, eastern California: An overview, *J. Geophys. Res.*, **90(B13)**, 11,111–11,120.
- Ide, S., and H. Aochi (2013), Historical seismicity and dynamic rupture process of the 2011 Tohoku-Oki earthquake, *Tectonophysics*, **600**, 1–13, doi:10.1016/j.tecto.2012.10.018.
- Johnson, L. (2010), An earthquake model with interacting asperities, *Geophys. J. Int.*, **182**, 1339–1373, doi:10.1111/j.1365-246X.2010.04680.x.
- Kaneko, Y., J.-P. Avouac, and N. Lapusta (2010), Towards inferring earthquake patterns from geodetic observations of interseismic coupling, *Nat. Geosci.*, **3**, 363–369, doi:10.1038/ngeo843.
- Kraft, T., A. Mignan, and D. Giardini (2013), Optimization of a large-scale microseismic monitoring network in northern Switzerland, *Geophys. J. Int.*, **195**, 474–490, doi:10.1093/gji/ggt225.
- Langbein, J. (2003), Deformation of the Long Valley Caldera, California: Inferences from measurements from 1988 to 2001, *J. Volcanol. Geotherm. Res.*, **127**, 247–267, doi:10.1016/S0377-0273(03)00172-0.
- Lay, T., and H. Kanamori (1981), An asperity model of large earthquake sequences, in *Earthquake Prediction, an International Review, Maurice Ewing Series*, vol. 4, edited by D. W. Simpson and P. G. Richards, pp. 579–592, AGU, Washington, D. C.
- Lienkaemper, J., and P. Williams (2007), A record of large earthquakes on the southern Hayward fault for the past 1800 years, *Bull. Seismol. Soc. Am.*, **97(6)**, 1803–1819, doi:10.1785/0120060258.
- Lienkaemper, J., P. Williams, and T. Guilderson (2010), Evidence for a twelfth large earthquake on the Southern Hayward fault in the past 1900 years, *Bull. Seismol. Soc. Am.*, **100(5A)**, 2024–2034, doi:10.1785/0120090129.
- Lienkaemper, J., F. McFarland, R. Simpson, R. Bilham, D. Ponce, J. Boatwright, and S. Caskey (2012), Long-term creep rates on the Hayward fault: Evidence for controls on the size and frequency of large earthquakes, *Bull. Seismol. Soc. Am.*, **102(1)**, 31–41, doi:10.1785/0120110033.
- Malservisi, R., K. Furlong, and C. Gans (2005), Microseismicity and creeping faults: Hints from modeling the Hayward fault, California (USA), *Earth Planet. Sci. Lett.*, **234**, 421–435, doi:10.1016/j.epsl.2005.02.039.
- Mignan, A. (2012), Functional shape of the earthquake frequency-magnitude distribution and completeness magnitude, *J. Geophys. Res.*, **117**, B08302, doi:10.1029/2012JB009347.
- Mignan, A., and G. Chouliaras (2014), 50 years of seismic network performance in Greece (1964–2013): Spatiotemporal evolution of the completeness magnitude, *Seismol. Res. Lett.*, **85**, doi:10.1785/0220130209.
- Mignan, A., and J. Woessner (2012), *Estimating the Magnitude of Completeness for Earthquake Catalogs, Community Online Resource for Statistical Seismicity Analysis*, doi:10.5078/corssa-00180805. [Available at <http://www.corssa.org/>.]
- Mignan, A., M. Werner, S. Wiemer, C.-C. Chen, and Y.-M. Wu (2011), Bayesian estimation of the spatially varying completeness magnitude of earthquake catalogs, *Bull. Seismol. Soc. Am.*, **101**, 1371–1385, doi:10.1785/0120100223.
- Mignan, A., C. Jiang, J. Zechar, S. Wiemer, Z. Wu, and Z. Huang (2013), Completeness of the Mainland China Earthquake Catalog and implications for the setup of the China Earthquake Forecast Testing Center, *Bull. Seismol. Soc. Am.*, **103**, 845–859, doi:10.1785/0120120052.
- Mori, J., and R. Abercrombie (1997), Depth dependence of earthquake frequency-magnitude distributions in California: Implications for rupture initiation, *J. Geophys. Res.*, **102(B7)**, 15,081–15,090.
- Mori, J., D. Wald, and R. Wesson (1995), Overlapping fault planes of the 1971 San Fernando and 1994 Northridge, California earthquakes, *Geophys. Res. Lett.*, **22**, 1033–1036.
- Noda, H., and N. Lapusta (2013), Stable creeping fault segments can become destructive as a result of dynamic weakening, *Nature*, **493**, 518–521, doi:10.1038/nature11703.
- Oncel, A., and M. Wyss (2000), The major asperities of the 1999 $M_w = 7.4$ Izmit earthquake defined by the microseismicity of the two decades before it, *Geophys. J. Int.*, **143**, 501–506, doi:10.1046/j.1365-246X.2000.00211.x.
- Ouillon, G., and D. Sornette (2011), Segmentation of fault networks determined from spatial clustering of earthquakes, *J. Geophys. Res.*, **116**, B02306, doi:10.1029/2010JB007752.
- Rippberger, J., J.-P. Ampuero, P. Mai, and D. Giardini (2007), Earthquake source characteristics from dynamic rupture with constrained stochastic fault stress, *J. Geophys. Res.*, **112**, B04311, doi:10.1029/2006JB004515.
- Sanders, C. (1993), Interaction of the San Jacinto and San Andreas fault zones, southern California: Triggered earthquake migration and coupled recurrence intervals, *Science*, **260**, 973–976, doi:10.1126/science.260.5110.973.
- Sanders, C., and H. Kanamori (1984), A seismotectonic analysis of the Anza seismic gap, San Jacinto fault zone, southern California, *J. Geophys. Res.*, **89(B7)**, 5873–5890.
- Schmidt, D., R. Burgmann, R. Nadeau, and M. d'Alessio (2005), Distribution of aseismic slip rate on the Hayward fault inferred from seismic and geodetic data, *J. Geophys. Res.*, **110**, B08406, doi:10.1029/2004JB003397.
- Scholz, C. (1968), The frequency-magnitude relation of microfracturing in rock and its relation to earthquakes, *Bull. Seismol. Soc. Am.*, **58(1)**, 399–415.

- Schorlemmer, D., and S. Wiemer (2005), Microseismicity data forecasts rupture area, *Nature*, **434**, 1086.
- Schorlemmer, D., S. Wiemer, and M. Wyss (2004a), Earthquake statistics at Parkfield: 1. Stationarity of b values, *J. Geophys. Res.*, **109**, B12307, doi:10.1029/2004JB003234.
- Schorlemmer, D., S. Wiemer, M. Wyss, and D. Jackson (2004b), Earthquake statistics at Parkfield: 2. Probabilistic forecasting and testing, *J. Geophys. Res.*, **109**, B12308, doi:10.1029/2004JB003235.
- Schorlemmer, D., S. Wiemer, and M. Wyss (2005), Variations in earthquake-size distribution across different stress regimes, *Nature*, **437**, doi:10.1038/nature04094.
- Shi, Y., and B. Bolt (1982), The standard error of the magnitude-frequency b value, *Bull. Seismol. Soc. Am.*, **72**, 1677–1687.
- Shirzaei, M., R. Burgmann, and T. Taira (2013), Implications of recent asperity failures and aseismic creep for time-dependent earthquake hazard on the Hayward fault, *Earth Planet. Sci. Lett.*, **371**, 59–66, doi:10.1016/j.epsl.2013.04.024.
- Sorey, M., V. McConnell, and E. Roeloffs (2003), Summary of recent research in Long Valley Caldera, California, *J. Volcanol. Geotherm. Res.*, **127**, 165–173, doi:10.1016/S0377-0273(03)00168-9.
- Spada, M., T. Tormann, S. Wiemer, and B. Enescu (2013), Generic dependence of the frequency-size distribution of earthquakes on depth and its relation to the strength profile of the crust, *Geophys. Res. Lett.*, **40**, 709–714, doi:10.1029/2012GL054198.
- Toppozada, T., D. Branum, M. Reichle, and C. Hallstrom (2002), San Andreas fault zone, California: $M \geq 5.5$ earthquake history, *Bull. Seismol. Soc. Am.*, **92**(7), 2555–2601.
- Tormann, T., S. Wiemer, and E. Hauksson (2010), Changes of reporting rates in the Southern Californian Earthquake Catalog, introduced by a new definition of ML, *Bull. Seismol. Soc. Am.*, **100**(4), 1733–1742, doi:10.1785/0120090124.
- Tormann, T., S. Wiemer, and J. Hardebeck (2012), Earthquake recurrence models fail when earthquakes fail to reset the stress field, *Geophys. Res. Lett.*, **39**, L18310, doi:10.1029/2012GL052913.
- Tormann, T., S. Wiemer, S. Metzger, A. Michael, and J. Hardebeck (2013), Size distribution of Parkfield's microearthquakes reflects changes in surface creep rate, *Geophys. J. Int.*, **193**(3), 1474–1478, doi:10.1093/gji/ggt093.
- Uhrhammer, R., M. Hellweg, K. Hutton, P. Lombard, A. Walters, E. Hauksson, and D. Oppenheimer (2011), California Integrated Seismic Network (CISN) local magnitude determination in California and vicinity, *Bull. Seismol. Soc. Am.*, **101**(6), 2685, doi:10.1785/0120100106.
- Vorobieva, I., C. Narteau, P. Shebalin, F. Beauducel, A. Nercessian, V. Clouard, and M.-P. Bouin (2013), Mapping of completeness magnitude of earthquake catalogs, *Bull. Seismol. Soc. Am.*, **103**, 2188–2202, doi:10.1785/0120120132.
- Waldhauser, F., and D. Schaff (2008), Large-scale relocation of two decades of northern California seismicity using cross-correlation and double-difference methods, *J. Geophys. Res.*, **113**, B08311, doi:10.1029/2007JB005479.
- Wdowinsky, S. (2009), Deep creep as a cause for the excess seismicity along the San Jacinto fault, *Nat. Geosci.*, **2**, 882–885, doi:10.1038/ngeo684.
- Wells, D., and K. Coppersmith (1994), New empirical relationships among magnitude, rupture length, rupture width, rupture area, and surface displacement, *Bull. Seismol. Soc. Am.*, **84**(4), 974–1002.
- Westerhaus, M., M. Wyss, R. Yilmaz, and J. Zschau (2002), Correlating variations of b values and crustal deformations during the 1990s may have pinpointed the rupture initiation of the $M_w = 7.4$ Izmit earthquake of 1999 August 17, *Geophys. J. Int.*, **148**(1), 139–152, doi:10.1046/j.0956-540x.2001.01554.x.
- Wiemer, S. (2000), Introducing probabilistic aftershock hazard mapping, *Geophys. Res. Lett.*, **27**, 3405–3408.
- Wiemer, S., and K. Katsumata (1999), Spatial variability of seismicity parameters in aftershock zones, *J. Geophys. Res.*, **104**, 13,135–13,151.
- Wiemer, S., and M. Wyss (1997), Mapping the frequency-magnitude distribution in asperities: An improved technique to calculate recurrence times?, *J. Geophys. Res.*, **102**, 15,115–15,128.
- Wiemer, S., and M. Wyss (2002), Mapping spatial variability of the frequency-magnitude distribution of earthquakes, *Adv. Geophys.*, **45**, 259–302.
- Wiemer, S., S. McNutt, and M. Wyss (1998), Temporal and three-dimensional spatial analyses of the frequency-magnitude distribution near Long Valley Caldera, California, *Geophys. J. Int.*, **134**, 409–421, doi:10.1046/j.1365-246x.1998.00561.x.
- Wiemer, S., D. Giardini, D. Faeh, N. Deichmann, and S. Sellami (2009), Probabilistic seismic hazard assessment of Switzerland: Best estimates and uncertainties, *J. Seismol.*, **13**, 449–478, doi:10.1007/s10950-008-9138-7.
- Woessner, J., and S. Wiemer (2005), Assessing the quality of earthquake catalogues: Estimating the magnitude of completeness and its uncertainty, *Bull. Seismol. Soc. Am.*, **95**, 684–698, doi:10.1785/0120040007.
- Wyss, M. (2001a), Locked and creeping patches along the Hayward fault, California, *Geophys. Res. Lett.*, **28**, 3537–3540.
- Wyss, M., and S. Wiemer (2000), Change in the probability for earthquakes in southern California due to the Landers magnitude 7.3 earthquake, *Science*, **290**, 1334–1338, doi:10.1126/science.290.5495.1334.
- Wyss, M., D. Schorlemmer, and S. Wiemer (2000), Mapping asperities by minima of local recurrence times: San Jacinto-Elsinore fault zones, *J. Geophys. Res.*, **105**, 7829–7844.
- Wyss, M., F. Klein, K. Nagamine, and S. Wiemer (2001), Anomalously high b -values in the south flank of Kilauea Volcano, Hawaii: Evidence for the distribution of magma below Kilauea's east rift zone, *J. Volcanol. Geotherm. Res.*, **106**, 23–27.
- Yang, W., E. Hauksson, and P. Shearer (2012), Computing a large refined catalog of focal mechanisms for southern California (1981–2010): Temporal stability of the style of faulting, *Bull. Seismol. Soc. Am.*, **102**(3), 1179–1194, doi:10.1785/0120110311.